

**Restricted**

**SR.15.11614**

**Mechanical characterization of Permian reservoir sandstone  
from the Moddergat-3 well in the Dutch Wadden Area**

**by**

**S. Hol (PTI/RF)**

**A.J. van der Linden (PTI/RF)**

**P.M.M. Zuiderwijk (PTI/RF)**

**F.H.M. Marcelis (PTI/RF)**

**A.H. Coorn (PTI/RF)**

This document is classified as Restricted. Access is allowed to Shell personnel, designated Associate Companies and Contractors working on Shell projects who have signed a confidentiality agreement with a Shell Group Company. 'Shell Personnel' includes all staff with a personal contract with a Shell Group Company. Issuance of this document is restricted to staff employed by a Shell Group Company. Neither the whole nor any part of this document may be disclosed to Non-Shell Personnel without the prior written consent of the copyright owners.

Copyright Shell Global Solutions International, B.V. 2015.

**Shell Global Solutions International B.V., Rijswijk**

Further electronic copies can be obtained from the Global Information Centre.

## **Executive summary**

The research reported here was carried out in the framework of the High Order Subsidence Monitoring (HOSM) project, supervised by the Royal Dutch Academy of Science (KNAW) and executed by NAM. In this contribution, we report on the effect of production-induced reservoir compaction, using core material from a Permian sandstone reservoir located at the Dutch Wadden Sea coastline, at a depth of  $\sim 3700$  m TVDMSL. To assess the nature of the compaction mechanisms that operate in these reservoirs, and hence better constrain predictions of subsidence rate and magnitude, we have carried out more than 30 long-term pore pressure depletion tests on sub-samples taken from the extracted core material. Our laboratory data show that pressure depletion results in total strain of  $5 \cdot 10^{-3}$  -  $15 \cdot 10^{-3}$  over the duration of the experiment of 5-12 weeks, with approximately 80% of the total strain response being close to instantaneous, and 20% time-dependent. The response is dependent on porosity and stress state, but is rather insensitive to temperature, and pore fluid composition. Our work shows that while volumetric compaction of the sandstone reservoirs could be responsible for the magnitude of the subsidence observed in the Wadden area, it cannot directly explain the observed temporal relationship between subsidence and reservoir pressure decline, or at least not without some rescaling factor. Instead, other mechanisms such as salt flow or water-leg compaction should also be considered.

## Table of contents

Executive summary	II
1. Introduction	1
2. Motivation and Background	2
3. Methods	4
3.1. Core material and pore fluid composition	4
3.2. Sample preparation and characterization	5
3.3. Experimental procedure	7
3.3.1. <i>Experimental systems</i>	7
3.3.2. <i>Uniaxial Pore Pressure Depletion (UPPD) – reference protocol</i>	9
3.3.3. <i>Uniaxial Pore Pressure Depletion (UPPD) – special protocols</i>	11
3.3.4. <i>Oedometeric loading at various rates (“Rate-type tests”) – special protocol</i>	12
3.3.5. <i>Stress-free Strain Pore Pressure Depletion (SSPPD) – special protocol</i>	13
3.3.6. <i>Triaxial compressive strength</i>	14
3.3.7. <i>Data processing</i>	15
3.3.8. <i>Microstructural analysis</i>	15
4. Results	16
4.1. Pore Pressure Depletion and Creep data	16
4.1.1. <i>Elastic constants derived from first loading</i>	17
4.1.2. <i>Axial strain and radial stress response to PPD</i>	18
4.1.3. <i>Axial stress hold – Uniaxial creep strain</i>	23
4.1.4. <i>Special protocols: Rate-type behavior and Stress-free strain conditions</i>	27
4.2. Triaxial compressive strength data	30
5. Discussion	32
5.1. Total compaction and elastic-inelastic strain partitioning	32
5.2. Deformation mechanisms responsible for inelastic strain	34
5.3. Role of lateral boundary conditions – strain versus stress control	40
5.4. Upscaling of laboratory tests	42
6. Conclusions	43
References	44
Appendix 1. CT-scans of the core in the barrels	45
Appendix 2. Selected sampling horizons	46
A2.1. Selected plug locations indicated in CT-scans of core material in barrels	46
A2.2. Core box number, depth and core length	47
Appendix 3. CT-scans and white light photos of the tested samples	48
Appendix 4. Porosity and permeability data for plugged intervals	58
Appendix 5. Mechanical data	59
Appendix 6. SEM images	60
A6.1. Sample 21 (pre) and 21A (post)	60

A6.2. Sample 22 (pre) and 22A (post)	61
A6.3. Sample 26 (pre) and 26E (post)	62
A6.4. Sample 27 (pre) and 27D (post)	63
A6.5. Sample 29 (pre) and 29D (post)	64
Bibliographic information	65
Report distribution	66

## 1. Introduction

Though depletion-induced reservoir compaction is a well-known phenomenon in the hydrocarbon industry, the mechanisms that operate, and the coupling between pressure decline and material response may strongly vary as a function of reservoir depth, composition, basin and production history, and material properties. Pressure solution creep, grain cracking, pore collapse, and shear failure are a number of possible operating mechanisms responsible for accommodating stress changes in the reservoir. In addition to these, upscaling of the response must be achieved in the lateral and stratigraphic directions, to arrive at a bulk description of the strain response, to serve as a means for bounding surface subsidence. Aside from the spatial component, also the temporal aspects must be addressed. A leading question in relation to the Wadden Area is whether the rate of subsidence, and hence reservoir compaction if this were considered the controlling mechanism, is higher than the natural sand infill rate controlled by tidal motion.

Here, we report the results of an experimental program executed in the years 2013-2015 that aimed at improving our understanding of the magnitudes, and rates, of reservoir compaction related to gas production from Dutch Wadden Sea fields. We describe a series of triaxial compressive strength, and uniaxial-strain pore pressure depletion (UPPD) tests, which enable us to assess the constitutive response of the Permian reservoir rock to production. We specifically investigate the role of pore fluid composition, temperature, in-situ stress magnitude, loading rate, and the effect of stress- versus strain-controlled lateral boundary conditions.

## 2. Motivation and Background

Dutch onshore and offshore operations have proven very productive over the last decades. The majority of the reservoirs are high-permeability, well-consolidated Aeolian sandstone formations in the West European Permian Basin. However, the ongoing production from these fields is resulting in subsidence. In the Wadden Sea, a tidal-flat area located between the North Sea and the Dutch mainland shore, a UNESCO World Heritage site, subsidence could potentially impact the ecological system. To guide the licensing process for the area by a good understanding of the system's response to production, the Dutch operator NAM has commenced a study on the magnitudes, timing, and causes of the observed subsidence. Within this program, steered by the Royal Dutch Academy of Sciences (KNAW), we address the effect of production-induced reservoir compaction, to assess the nature of the compaction mechanisms that operate. We ultimately aim to quantify the inter-reservoir strain response to depletion, and describe the constitutive behavior in terms of material properties and boundary conditions, in order to improve bounds on predictions of subsidence rate and magnitude.

Important input used to date in the modelling of the subsidence observed in the Groningen and Wadden Areas, is the uniaxial compressibility  $C_m$  that expresses the reservoir strain response per unit pore pressure decline. The origin of this parameter is in the analytical work by Geertsma [1, 2] who estimated the shape and magnitude of a subsidence bowl, based on a nucleus-of-strain approach in an elastic half-space. The classical model considers a disc-shaped reservoir with thickness  $b$  and radius  $r$  at depth  $D$ , subjected to a uniform pore pressure change  $\Delta P_p$ , and expresses the vertical displacement  $u_z$  of the surface as [3],

$$u_z(r, 0) = -\frac{1}{\pi} C_m (1 - \nu) \frac{D}{(r^2 + D^2)^{\frac{3}{2}}} \cdot \Delta P_p \cdot V$$

where  $\nu$  is the Poisson's ratio,  $V$  is a small finite reference volume. The elastic parameters are assumed to be constant throughout the complete half-space. Vertical displacement  $u_z$ , *i.e.* surface subsidence, can now be estimated to within an order-of-magnitude by 1) taking the reservoir dimensions as known from the field, and 2) experimentally determining the magnitude of the "elastic" parameter  $C_m$ . Previous experimental campaigns within Shell have indeed focussed on assessing the magnitude of the compressibility  $C_m$  via Pore Pressure Depletion (PPD) tests, and yielded values in the range  $0.2 \cdot 10^{-5}$ - $8.9 \cdot 10^{-5}$  bar<sup>-1</sup> for the Wadden region (Fig. 1). The obtained  $C_m$ -values vary per reservoir, and are dependent on porosity, but also on the test procedure chosen.

Despite the success of the practical model developed by Geertsma [1, 2], the assumption that reservoir material is truly homogenous and fully elastic, is highly questionable for these sandstones from a geological and rock constitutive perspective. Granular aggregates in geological formations always display variation in packing, grain composition, strength and frictional properties. This highlights a central problem in upscaling and motivates a detailed experimental study with focus on the recoverability of deformation, and time-dependent aspects, geared at developing accurate understanding of the variability of the reservoir material response, and providing this information to the general public via the State Supervision of Mines (SodM).

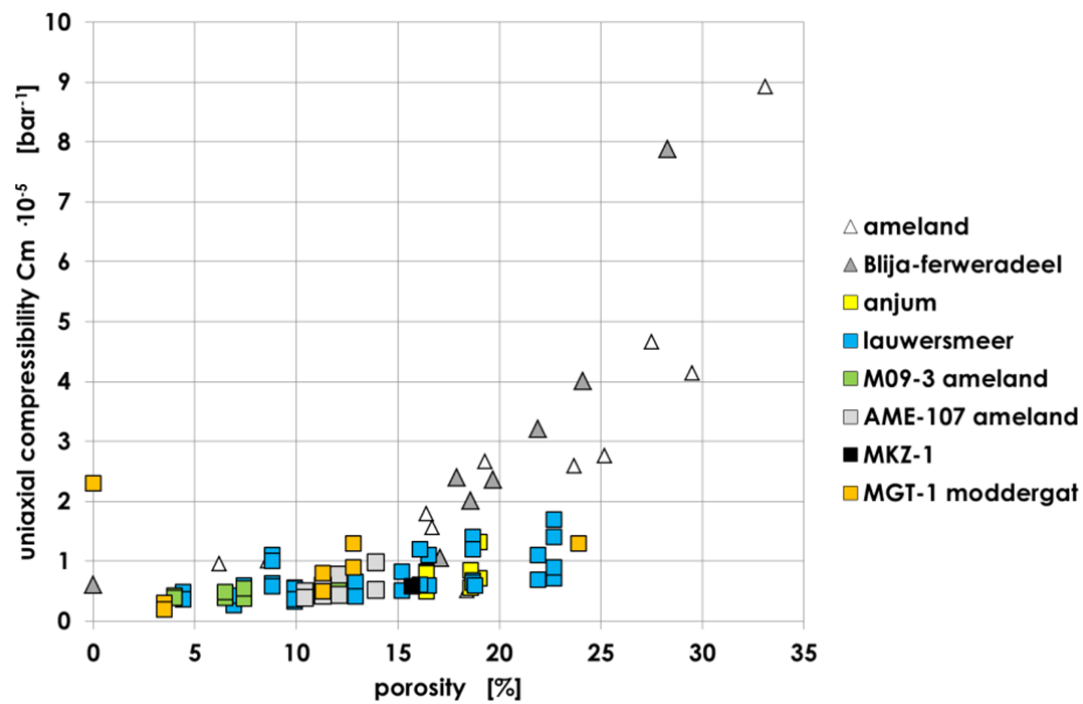


Fig. 1. Uniaxial compressibility  $C_m$  versus porosity for samples extracted from wells near the Moddergat-3 well investigated in this study.

### 3. Methods

To investigate the constitutive behavior of Permian reservoir sandstones, in particular the magnitude of the strain response to stress changes, and their temporal nature, we carried out a large number of triaxial and UPPD tests using plug samples. Prior to testing, the sample material was characterized for basic granular and flow properties. Conditions imposed during the mechanical experiments were chosen consistent with the changes in stress, pressure and temperature expected during production from the Moddergat well. We adopt the convention that compressive stresses and strains are positive.

#### 3.1. Core material and pore fluid composition

Core material was extracted from the Moddergat-3 well (Nes Field) located at the Wadden Sea coastline, at a depth of  $\sim 3700$  m TVDMSL. In-situ stress and pore pressure magnitudes, as well as the expected pore pressure at maximum depletion conditions, were provided by T. Mossop (NAM/PTU/E/Q), and are listed in Table 1. The reservoir pressure  $P_p$  in the partially produced reservoir was  $\sim 42$  MPa at the time of coring, whereas in the ‘virgin’ state, the pressure was  $\sim 57$  MPa, vertical stress  $S_v$  was 80 MPa, and horizontal stresses  $S_{Hmax}$ ,  $S_{Hmin}$  close to 67 MPa. These stresses were taken as representative for the field throughout the present study, and will be referred to further as “in-situ stress”. The pore pressure used is the pressure in the virgin state.

**Table 1: Moddergat-3 in-situ stress data.**

	<b>Stress [MPa]</b>
Vertical stress	80
Horizontal stress	67
Pore pressure – virgin	57
Pore pressure – time of coring	42
Pore pressure – expected when fully depleted	3

The core had a diameter of 4 inch, and was approximately 100 m long. After coring, it was transported in aluminum inner barrels to the Shell Core Repository in Rijswijk, the Netherlands, to be processed. CT scans were made per barrel of the full length of the core to identify apt sub-sampling locations. These scans are provided in Appendix 1.

In-situ formation brine compositions were adopted from the Land North/Groningen formation water database, and provided by Jan-Willem Kruse (NAM-UIO/T/SH). Based on the compositional data, synthetic brine was prepared and stored for experimental testing of those samples that used brine as a pore fluid.

**Table 2: Moddergat-3 synthetic brine composition.**

<b>salt</b>	<b>Concentration [g.l<sup>-1</sup>]</b>
NaCl	205.7
KCl	4.3
CaCl <sub>2</sub> .2H <sub>2</sub> O	0.1
MgCl <sub>2</sub> .6H <sub>2</sub> O	19.6

It is well-known that aqueous fluids have the potential of assisting deformation mechanisms, e.g. via stress corrosion cracking, or pressure solution creep. To isolate the effects of these mechanisms, control experiments will be conducted using non-aqueous fluids (oils). Based on the viscosity similarity with brine, Morlina-5 and Dodecane were selected. Morlina-5 is a paraffinic mineral oil with a density of  $0.84 \text{ g}\cdot\text{cm}^{-3}$  and a viscosity of  $2.2 \text{ mPa}\cdot\text{s}$  at  $60 \text{ }^\circ\text{C}$ , while n-Dodecane is a liquid alkane hydrocarbon  $[\text{CH}_3(\text{CH}_2)_{10}\text{CH}_3]$  with a density of  $0.75 \text{ g}\cdot\text{ml}^{-1}$  and a viscosity of  $1.34 \text{ mPa}\cdot\text{s}$  at  $25^\circ\text{C}$ . However, the use of n-Dodecane is not recommended at higher temperatures, as it has a flashpoint of  $83 \text{ }^\circ\text{C}$ , and hence we restricted use to one experiment at room temperature.

### 3.2. Sample preparation and characterization

From the intervals selected based on the CT scans (refer to Section 3.1, and Appendix 2), three to five plugs measuring 1.0 and 1.5 inch in diameter, 2.0 and 3.0 inch in length respectively, were drilled using the prepared synthetic brine, or oil, as a cooling fluid (for CT scans and images refer to 0). The samples were then stored in the fluid chosen for drilling. The samples measuring 1.5 inch in diameter were used only for UPPD tests, whereas sample measuring 1.0 inch in diameter were used for triaxial and UPPD testing. Note that care was taken to systematically vary porosity, and sample morphology, to ensure a proper representation of the reservoir material variability.

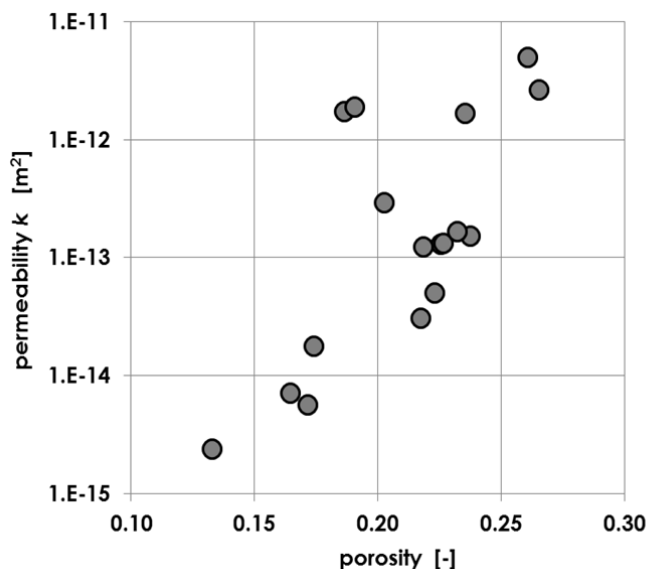


**Fig. 2. Permeability versus porosity for the complete sample set used in the present study. The average porosity and permeability for the rock considered are  $\sim 0.2$  and  $\sim 10^{-13} \text{ m}^2$  ( $\sim 0.1 \text{ D}$ ) respectively.**

For each horizon sampled, we determined the bulk and solid phase volume by immersing a sample in Hg and chloroform respectively. Permeability to  $\text{N}_2$  was determined on the same plugs at a constant confining pressure of  $2.75 \text{ MPa}$  ( $400 \text{ psi}$ ), and plotted in Fig. 2 versus porosity for the complete sample set. Porosities were in the range  $0.14$ - $0.27$ , and showed a positive correlation with permeability in the range  $\sim 10^{-14} \text{ m}^2$  (low-end porosities) to  $\sim 10^{-11} \text{ m}^2$  (high-end porosities). All porosity and permeability data are listed in Appendix 4. Laser particle size analysis (Fig. 3) on strips of disaggregated material, taken next to the plugs, yielded a size distribution with a small silt/clay fraction, and a clear log-normal ( $R^2 > 0.99$ ) distribution of particles between  $50 \text{ }\mu\text{m}$  and  $1 \text{ mm}$  in diameter. These comprise primarily quartz grains. The mean grain size in the measured samples ranges from  $230$ - $360 \text{ }\mu\text{m}$ , and widths of the log-normal peak between  $0.32$  and

0.65. These properties are roughly correlated with porosity, suggesting slight packing differences (Fig. 4). Low porosity samples tend to constitute a broader grain size distribution that supports a larger mean grain size.

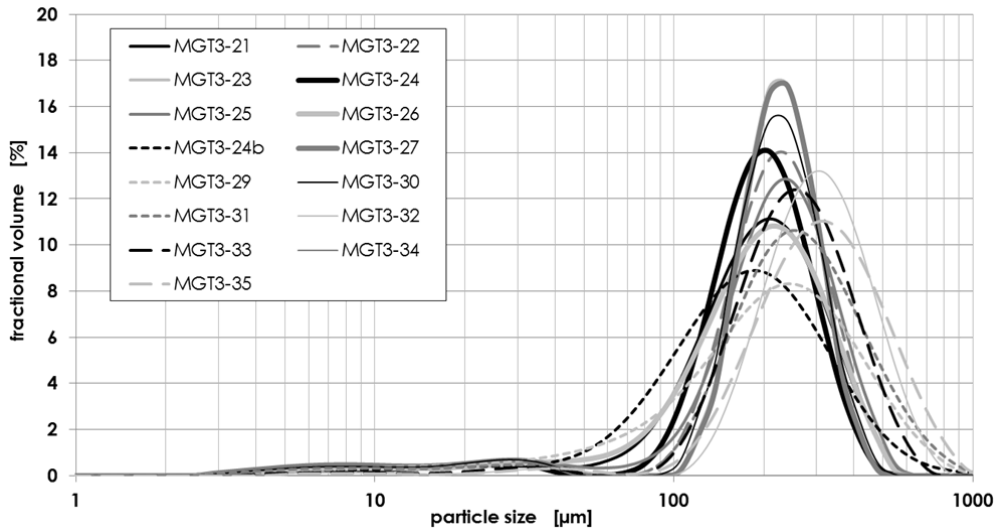


Fig. 3. Particle size distribution for selected individual samples used in the present study. The peak in the range 50-1000 µm can be parameterized using a log-normal fit, with  $R^2 > 0.99$ .

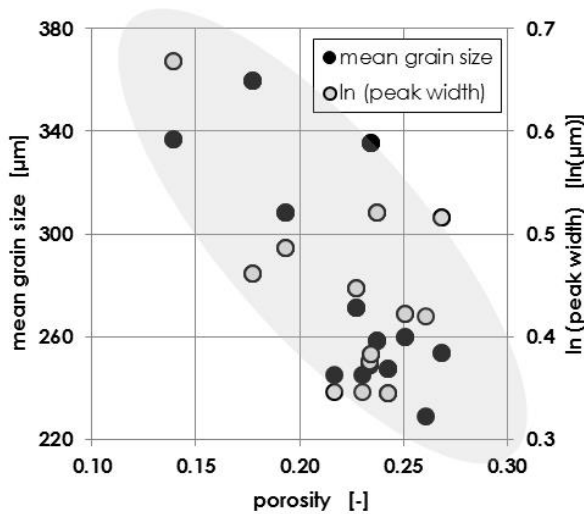


Fig. 4. Mean grain size and peak width versus porosity for the sample set used in the present study.

### 3.3. Experimental procedure

To assess the nature of the compaction behavior, and describe the grain-scale failure mechanisms, during depletion of the Permian sandstone reservoir extracted from the Moddergat-3 well, we employ triaxial pressure vessel with the capability of measuring compaction under the boundary conditions relevant to in-situ condition, both in terms of magnitude and orientation. We made a general assumption that the boundary condition of uniaxial strain, i.e. zero-lateral strain, applied in a step-wise manner, is the most representative for the field conditions. Nonetheless, we have also chosen to carry out a number of experiments under special boundary conditions, namely a) higher and lower axial stress during depletion, b) one-step depletion, c) varying loading rate, d) stress-free strain conditions. In addition, we have performed a suite of triaxial compressive strength tests, and we will handle in the discussion their connection with the result obtained from the UPPD tests. Next we will discuss the experimental system utilized, and the specific stress paths employed.

#### 3.3.1. Experimental systems

A range of triaxial pressure vessels was used for performing compressive strength and UPPD tests. All systems, located in the Shell Geomechanics Laboratory in Rijswijk, the Netherlands, operate using independent hydraulic pump systems, with pressures limited at a maximum of 110 MPa. Examples of our systems are presented in Fig. 5 and Fig. 6.

In the case of the Petrophysical Rock Properties cell, a cylindrical sample can be mounted onto the titanium end caps, enclosed in an impermeable 2.5 mm-thick Viton® sleeve, and is then loaded axially by applying oil pressure in the chamber below the loading piston using a hydraulic actuator. Pressure is measured using a 100 MPa pressure gauge and controlled to within 0.1 MPa by a custom analog servo-controller. Radial stress is applied directly to the sample through oil pressure on the sleeve using a similar piston (hydraulic) actuator, pressure gauge, and controller. The in- and outlet can be pressure-controlled, so that the sample can be saturated with fluid at pore pressure  $P_p$ . Changes in the sample length are measured using the relative vertical displacement of two Invar rods in contact with the end caps through concentric bores drilled in the bottom piston and top plate of the pressure vessel. A rectangular Invar frame, suspended independently of the vessel, transmits the relative movement of the rods to a linear variable displacement transducer (LVDT) located under the pressure vessel. In this way, the axial shortening and extension of the sample plus end caps is measured. During signal processing, the raw axial displacement data are actively corrected for the axial deformation of the end caps due to axial and radial loads and temperature changes. The change in the diameter of the sample is measured using a strain-gauged cantilever bridge. The bridge is positioned at the center of the sample. The sensor is clamped onto two pins that pierce the elastomer sleeve, making direct contact with the sample at opposite sides. During loading under uniaxial constant-lateral strain conditions, the total radial stress is varied to maintain a constant radial dimension using the above-mentioned servo-controller, and include corrections for pressure effects on the radial sensor. Calibration experiments on aluminum samples show that the radial displacement under uniaxial constant-strain conditions can be maintained within  $\pm 1$  microns ( $\pm 0.05$  millistrain). Strains were measured both in the axial and radial directions; axial strain using LVDT's, and radial strains using a two-pin, strain gage based system in direct coupling with the sample via jacket punctures and pins at the center of the sample. Care was taken to position these pins in the dip-direction of the inclined Aeolian cross-bedded material, aiding the radial position control during pore pressure depletion under uniaxial strain conditions. Temperature was measured in the pressure lines, as well as in the pressure vessel, and controlled using either an oven, or an internal heating system.

The quadruple system presented in Fig. 6 was specially designed and built for the purpose of the present study, and consists of four pressure vessels that are operated in a manner similar to the operation of the PRP cell. However, the quadruple system can hold samples 1.0" in diameter only, and temperature control is achieved by means of brass elements attached to the sleeve.

All experiments were carried out in a fully automated, pc-controlled manner, following a pre-programmed triaxial stress or uniaxial strain path. Note that apparatus stiffness and thermal corrections are taken into account in all active control systems during operation (*e.g.* when controlling radial strain by means of the confining pressure), as well as in processing the logged data.

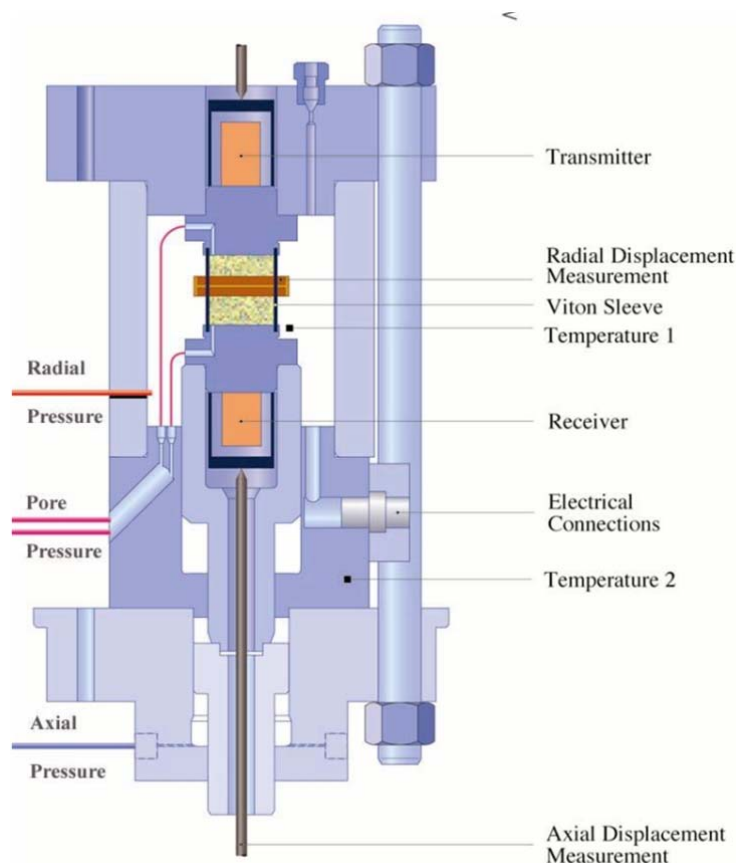


**Fig. 5. Schematic diagram of a triaxial pressure vessel referred to as the Petrophysical Rock Properties (PRP) cell, used to perform triaxial compressive strength measurements. The cell can hold 1"-1.5" diameter samples, and is capable of measuring ultrasonic travel time (P, S waves). Similar standalone systems were used in course of this study, of which two could be heated in an external oven up to 120 °C.**

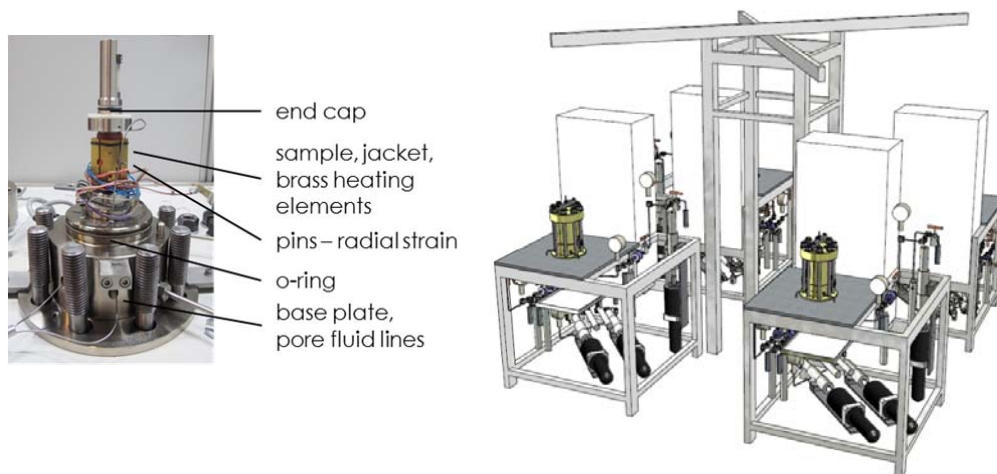


**Fig. 6. Quadruple system developed within the scope of the present research project. In all four triaxial pressure vessels, axial, radial and pore pressure can be controlled independently. Temperatures up to 120 °C can be generated using brass heating elements inside the vessel.**

### *3.3.2. Uniaxial Pore Pressure Depletion (UPPD) – reference protocol*

UPPD tests were performed on a suite of samples with a range of porosities, taken primarily from the production interval. A sample was mounted in the compaction cell as received, and loaded to an axial stress of 1.5 MPa and a radial stress of 1.0 MPa, after which a pore pressure of 0.5 MPa was applied. The sample was then flushed with approx. 6 pore volumes of pore fluid (brine, Morlina- or n-dodecane), at a pressure between 1.0 MPa and 1.5 MPa, to ensure complete saturation and removal of air from sample and capillary tubing.

The test procedure for the UPPD experiments can be divided into four stages:

- 1) Loading to in-situ stress conditions
- 2) Consolidation at the restored in-situ stress conditions
- 3) Pore pressure depletion
- 4) Creep

Stage 1 and 2 were carried out under triaxial stress conditions, while stage 3 and 4 were carried out under uniaxial strain conditions. Loading rates were 1.0 MPa.hr<sup>-1</sup> in all cases.

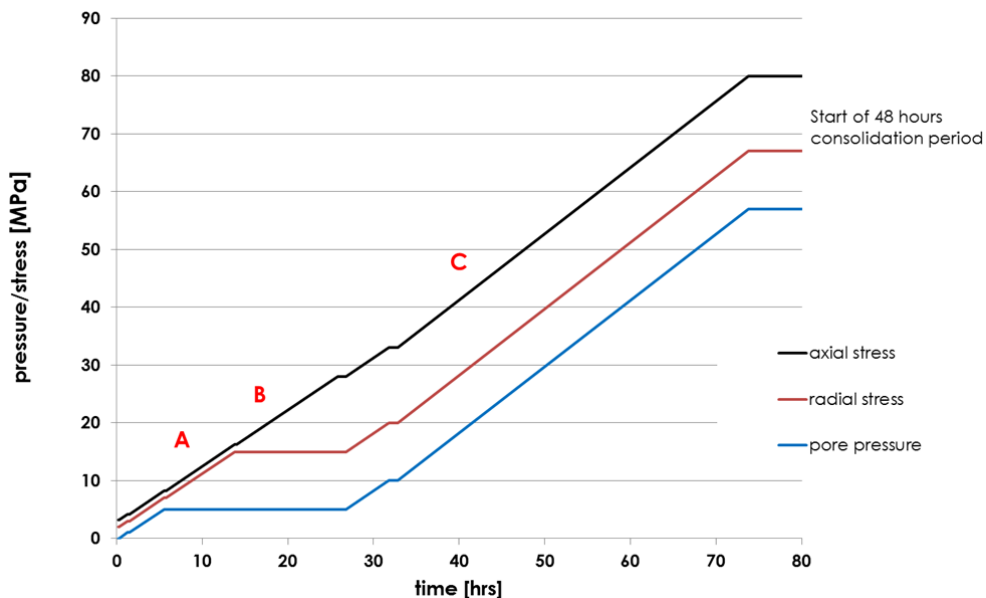


**Fig. 7. Loading path to in-situ conditions of stress and pore pressure. The three segments indicated yield the A) Bulk modulus  $K_b$ , B) Young's Modulus  $E$  and Poisson's ratio  $\nu$ , and C) Solid phase or Grain modulus  $K_s$ .**

#### 1) Loading to in-situ stress:

The samples were first brought to in-situ conditions of pressure, and stress (refer to Section 3.1), at a temperature  $T$  of 20, 60 or 100 °C, and settled for a couple of days. Fig. 7 shows a detailed overview of the procedure, and defines loading segments, namely Isostatic loading (A), Axial loading (B) and Constant Net Stress loading (C), from which baseline rock mechanical parameters can be determined. During Step A, the axial and radial stresses were increased from 8 MPa to 15 MPa while the pore pressure was held constant at 5 MPa, to determine the bulk modulus  $K_b$  from the change in volumetric strain and the change in mean effective stress. Following, during Step B, the axial stress was increased to 28.4 MPa while the radial stress and pore pressure were kept constant at 15 MPa and 5 MPa, respectively. Young's modulus and Poisson's ratio were determined using the change in axial strain, radial strain and axial effective stress. At these effective in-situ stress conditions, the sample was heated to the anticipated test temperature. Tests were conducted at room temperature, 60 °C and 100 °C. For experiments executed at room temperature, the heating step was skipped. Once satisfactory equilibration to temperature was achieved, Step C was started, in which the axial and radial stress and pore pressure were increased simultaneously with the same rate to the original in-situ total stresses. Note, that effective stress on the sample remained the same. From the data, the solid phase or grain modulus  $K_s$  can be derived using the change in volumetric strain as a function of change in pore fluid pressure. Finally, the sample was mechanically equilibrated for at least 48 hours.

#### 2) Settling at the restored in-situ stress conditions

Following loading, the sample was held at in-situ conditions for at least 48 hours to allow for mechanical settling and equilibration.

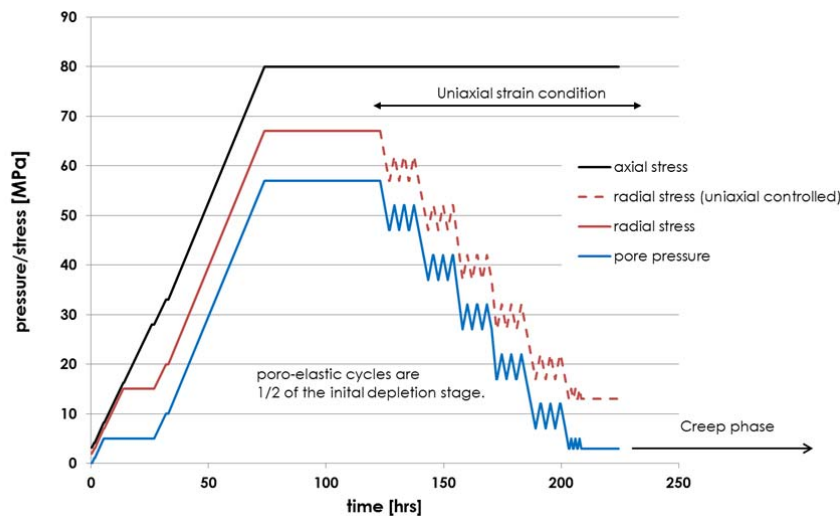


**Fig. 8. Axial stress, radial stress and pore pressure as a function of time for the uniaxial pore pressure depletion experiments with multiple inflation/depletion cycles**

### 3) Pore Pressure Depletion:

Once stable, the pore pressure decreased in cycles, under actively controlled lateral constraint boundary conditions (*i.e.* uniaxial strain), until maximum depletion at 3 MPa pore pressure is achieved (Fig. 8). The loading rate for all depletion steps and inflation/depletion cycles was  $2.5 \text{ MPa}\cdot\text{hr}^{-1}$ . Each full depletion cycle took approximately 7 days, and was carried out in steps of 10 MPa, or 4 MPa. Each depletion step was followed by three 5 MPa inflation/depletion cycles under uniaxial strain conditions. The depletion step and inflation/depletion cycles were repeated five times until a  $P_p$  of 3 MPa was reached (anticipated maximum depletion pore pressure). Note that in the last step, a depletion step of 4 MPa was performed (from 7 MPa to 3 MPa) followed by three 2 MPa inflation/depletion cycles. The inflation/depletion cycles allow for assessing the elastic response at that particular step, in order to separate elastic and inelastic strains.

### 4) Creep:

After reaching  $P_p = 3 \text{ MPa}$ , the stress and uniaxial strain conditions were maintained for a creep period of at least 350 hours to monitor axial compaction and radial stress changes as a function of time (Fig. 8). The last 72 hours of the creep period were performed in stress control (*i.e.* no uniaxial strain control) to monitor, axial and radial strain changes. Finally, the sample was unloaded and allowed to cool to ambient conditions. A number of experiments were conducted with creep periods up to  $\sim 8$  months to monitor ultimate settling behavior.

#### 3.3.3. *Uniaxial Pore Pressure Depletion (UPPD) – special protocols*

##### Lower and higher in-situ stresses:

In the test with sample MGT3-26D, the sample was loaded to stress conditions 5 MPa higher than the original in-situ stress conditions. By contrast, sample MGT3-26C was loaded to stress conditions 5 MPa lower than the original in-situ stress conditions. The pore pressure depletion steps and inflation/depletion cycles had the same amount of depletion per step or cycle as in the original stress path. The depletion, inflation depletion cycles and the subsequent creep phase were also executed under uniaxial strain conditions.

### One-step depletion:

Depletion in the UPPD tests using samples MGT3-29D, MGT3-32D, MGT3-33C and MGT3-34C was achieved in a single step from 57 MPa to 3 MPa, at a pressure rate of  $2.5 \text{ MPa}\cdot\text{hr}^{-1}$  (Fig. 9). The axial stress was kept constant throughout the hold and depletion stages.

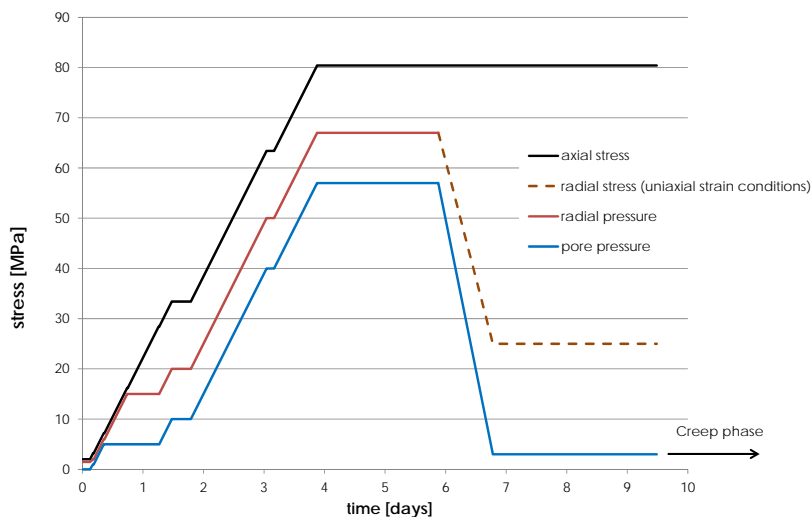


**Fig. 9. Stress path for one-step depletion experiments showing axial stress, radial stress and pore pressure as a function of time.**

### 3.3.4. Oedometeric loading at various rates ("Rate-type tests") – special protocol

To investigate the effect of loading rate on the constitutive behaviour of selected, representative samples under uniaxial strain control, two tests were performed where the axial stress was increased and decreased in steps using different loading rates to the effective axial stress state at maximum depletion conditions (Fig. 10). After an initial poroelastic loading cycle, the tests were performed under fully saturated but drained conditions with the pore lines open to air. Of the two tests, one was performed at room temperature, and one at  $60 \text{ }^\circ\text{C}$ .

The sample was loaded to  $S_{ax} = 16 \text{ MPa}$ ,  $P_{rad} = 15 \text{ MPa}$  and  $P_p = 5 \text{ MPa}$ . Then, the pore pressure was lowered to  $0.1 \text{ MPa}$  while  $S_{ax}$  and  $P_{rad}$  were concomitantly raised to  $33 \text{ MPa}$  and  $20 \text{ MPa}$ , respectively. The valve of the pore system was opened to air so that drained conditions were created with zero pore pressure. In the test at  $60 \text{ }^\circ\text{C}$ , the temperature was raised at these stress conditions. After consolidation to the new stress and temperature conditions, two axial unload/load cycles were performed to measure the inelastic and elastic strain components. The axial stress was increased to  $76.2 \text{ MPa}$  in six steps. In these steps, the axial stress rates varying three orders of magnitude were applied, in the sequence:  $0.3 \text{ MPa}\cdot\text{hr}^{-1} \rightarrow 3 \text{ MPa}\cdot\text{hr}^{-1} \rightarrow 0.3 \text{ MPa}\cdot\text{hr}^{-1} \rightarrow 30 \text{ MPa}\cdot\text{hr}^{-1} \rightarrow 0.3 \text{ MPa}\cdot\text{hr}^{-1} \rightarrow 3 \text{ MPa}\cdot\text{hr}^{-1} \rightarrow 0.3 \text{ MPa}\cdot\text{hr}^{-1} \rightarrow \text{etc.}$ . After consolidation at  $76.2 \text{ MPa}$  for  $48 \text{ hr}$ , unloading was achieved similarly but in reverse. Three axial unloading/loading cycles were performed to determine elastic constants.

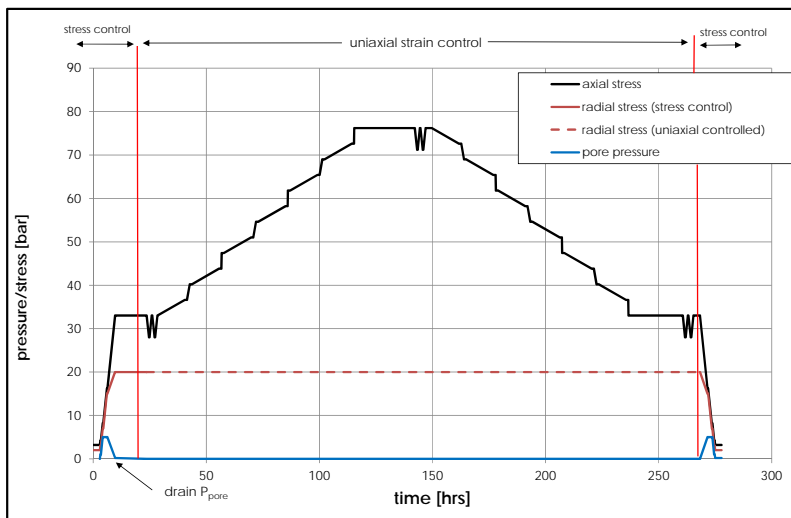


**Fig. 10. Stress-path “Rate-type” tests showing axial stress, radial stress and pore pressure as a function of time, both in triaxial stress control and uniaxial strain control.**

*3.3.5. Stress-free Strain Pore Pressure Depletion (SSPPD) – special protocol*

Two experiments were performed under so-called ‘stress free strain’ conditions, *i.e.* where the external sample stress state remains unperturbed while the sample undergoes its intrinsic volume strain caused by pore pressure decrease, with the aim to establish deviations from isotropic, linear-elastic behavior (Fig. 11). Following Stages 1 and 2 described in Section 3.3.2, the axial and radial stress were kept **constant** at in-situ stresses (80 MPa and 67 MPa respectively) while the pore pressure was decreased in a stepwise manner. Similar to the depletion steps described for the reference protocol, each depletion step of 10 MPa pore pressure reduction was followed by three 5 MPa inflation/depletion cycles. The depletion step and inflation/depletion cycles were repeated five times until a  $P_p$  of 3 MPa was reached. After reaching  $P_p = 3$  MPa, the stresses were maintained for a creep period to monitor volumetric compaction as a function of time, after which the sample was unloaded. The experiment was conducted at room temperature.

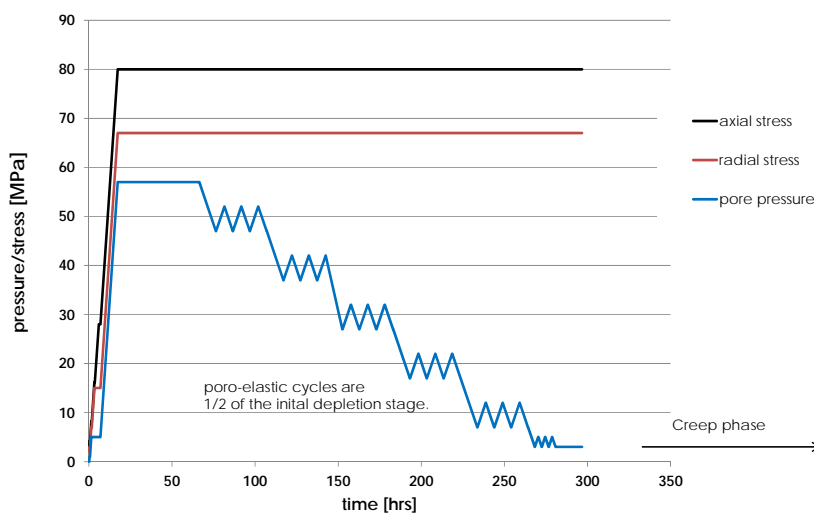


**Fig. 11. Stress path Stress-free Strain Pore Pressure Depletion (SSPPD) showing axial stress, radial stress and pore pressure as a function of time**

### 3.3.6. Triaxial compressive strength

Triaxial tests were performed using two sets of samples with porosities of 0.14 (Sample set MGT-24) and 0.27 (Sample set MGT-29) respectively, using three different confining pressures per set (Fig. 12). These confining pressures were chosen for the sample 24-series as roughly 0.5, 1 and 1.25 times, and for the 29-series roughly 0.25, 0.5, and 1.25 times the virgin mean effective stress (VMES). These porosities of the samples sets roughly resemble end-member cases within the Permian reservoir sandstone considered here (Fig. 2), which allows us to roughly later interpolate the results obtained. All experiments are executed at room temperature. Prior to testing, the samples were saturated with brine.

Each experiment starts by subjecting the sample to an axial stress of 2.7 MPa and a radial stress of 2.0 MPa. A pore pressure of 1.0 MPa was applied. Hereafter, the samples were taken to the initial mean effective stress state (e.g.  $S_{ax} = S_{rad} = 12.1$  MPa and  $P_p = 5$  MPa) and followed, depending on the mean effective stress of the test, by one, two or three isostatic stress cycles with an axial and radial stress cycle of 4 MPa. After a consolidation period, the axial stress was increased at the strain rate of  $2 \cdot 10^{-6} \text{ s}^{-1}$  while radial stress and pore pressure were kept constant until failure is achieved. Bulk modulus, compressive strength, friction angle and cohesion can be determined from the stress-strain tangent during loading. Ultrasonic axial compressional and shear wave travel times were measured by the pulse-transmission technique, and recorded at intervals of several minutes, to compute compressional and shear wave velocities.

After failure of the sample, the axial stress is unloaded to the radial stress following an isostatic unloading to ambient conditions. In addition to the tests using the end-member sets and brine as a pore fluid, two experiments were performed on samples saturated with non-aqueous fluid. These tests were also carried out at room temperature.

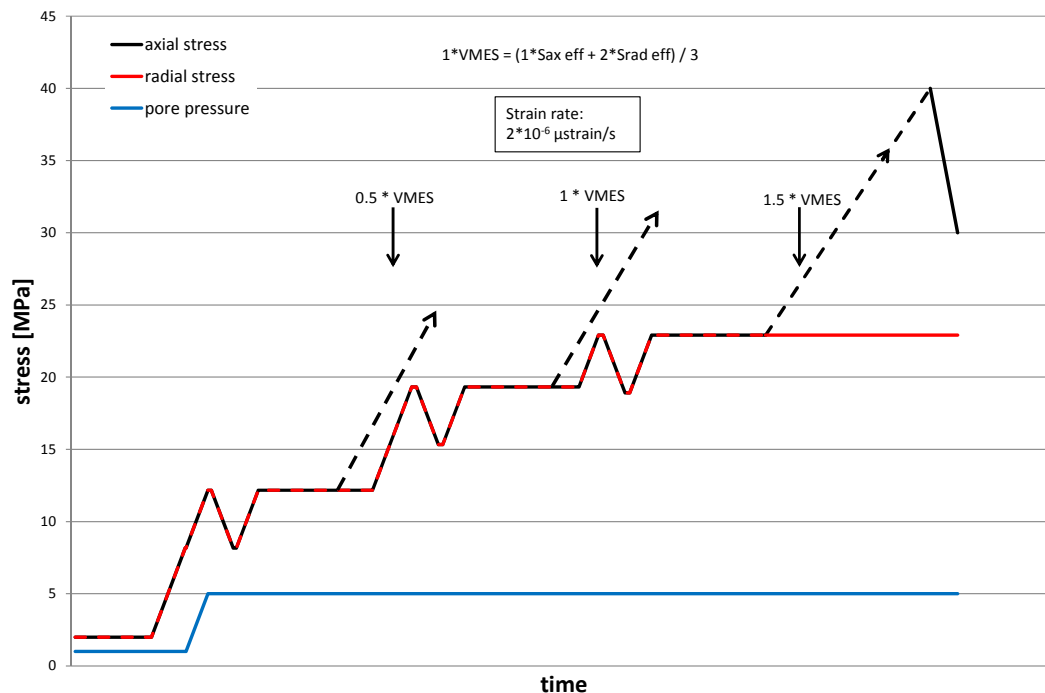


Fig. 12. Stress path for triaxial compressive strength tests showing the change in axial stress, radial stress and pore pressure as a function of time.

### *3.3.7. Data processing*

Data were acquired at 12 bit resolution and logged using a pc. Axial stress, radial stress and pore pressure, as well as axial and radial displacements are recorded continuously during an experiment. From these data, static elastic properties were determined from the slopes of stress-strain curves for each loading and unloading step (averaged over the loading/unloading time, not including the creep phase unless otherwise noted). This included Young's moduli, the Poisson's ratio, uniaxial compaction coefficient  $C_m$  and the depletion constant  $\gamma = \Delta S_{rad} / \Delta P_{pore}$ . From the shear failure data, friction angle and cohesion are determined.

### *3.3.8. Microstructural analysis*

Five intervals in the gas-filled part of the reservoir were selected for microstructural analysis using Scanning Electron Microscopy (SEM). To compare pre- and post-testing states, we took the center piece of the skeleton of the core material after drilling the plug samples as representative of the pre-testing state, and the plug samples after the experiments as representative for material post-testing. It was ensured that individual layers in the samples matched the layers inside the skeleton piece. Sections were taken vertically in the dip direction, filled with epoxy resin, and polished. A qualitative comparison was made of the sample material before and after mechanical testing, which we will address further in Section 5.2.

## 4. Results

The results of more than 30 UPPD tests and triaxial compressive strength tests are presented in Fig. 13-Fig. 32, post-testing images are provided in Appendix 6, and a detailed overview of experiments and experimental conditions is provided in Appendix 4. The UPPD data will be described in Section 4.1 and the triaxial compressive strength data in Section 4.2. In the discussion that follows in Section 5, we will discuss correlations in these data sets, but also introduce one additional data set that connects the UPPD conditions and bounding triaxial compressive strength. Note that several mechanical tests have failed as a result of technical issues with the radial stress and strain control (e.g. sample 21B, see Appendix 3). The resulting measurements were isolated from the data set and used for improving technical capability only, i.e. they are not reported specifically in this report.

### 4.1. Pore Pressure Depletion and Creep data

In total, more than 30 UPPD tests were performed using brine, Morlina-5 or Dodecane, at a temperature of 20°C, 60°C or 100°C, and employing various stress paths. All UPPD tests were carried out following a protocol with four stages, as described in Sections 3.3.2 to 3.3.5. Stages 1-2 were conducted under triaxial conditions, and yield poroelastic constants, and Stages 3-4 under uniaxial strain boundary conditions. We plot in Fig. 6 again a stress path, as well as the axial strain and radial stress response for a representative sample. Below, we will describe these results, and the trends observed in the full data set. We focus on the effects of sample and fluid properties on the elastic and inelastic constitutive response.

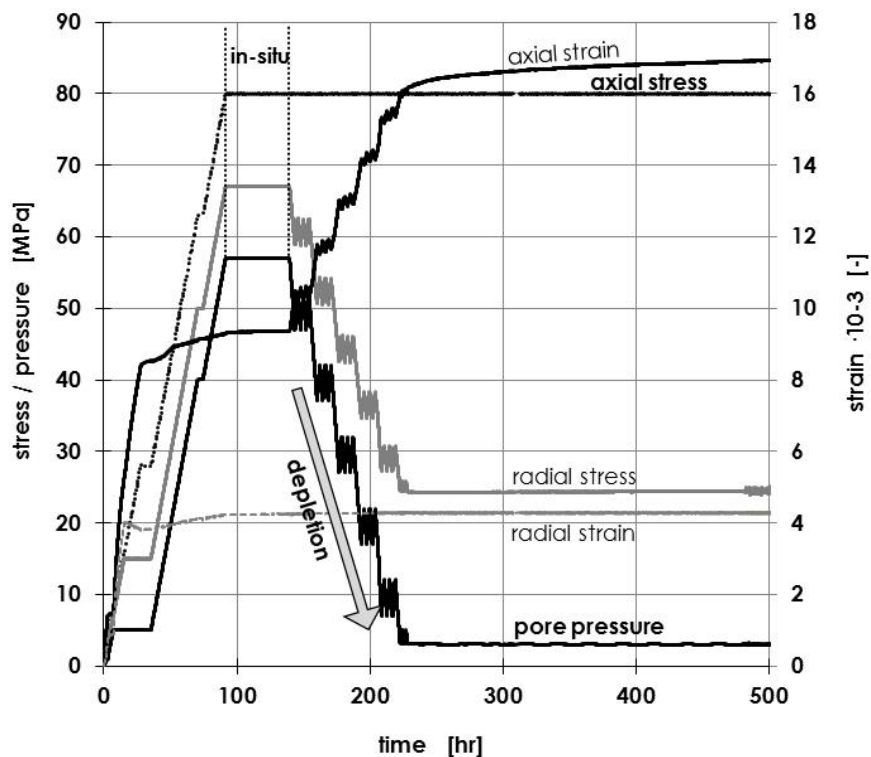


Fig. 13. UPPD test reference stress path, and representative constitutive response, in this case sample MGT-22A. The sample is brought to virgin in-situ stress, and subjected to a decrease in pore pressure while maintaining constant axial stress, and radial strain. Measured responses are the axial strain, and radial stress. Note the small relative contribution of time-dependent strain during the final hold period.

#### 4.1.1. Elastic constants derived from first loading

Loading to in-situ conditions of 3D stress and pore pressure resulted in estimates of the (poro)elastic constants for the material tested. A bulk modulus  $K_b$  was determined for all samples tested during isostatic loading (Segment A - Fig. 7), and yields an average value of  $0.9 \pm 0.2$  GPa. No relationship is observable between porosity and bulk modulus. By contrast, axial loading (Segment B - Fig. 7) that then followed, yields Young's moduli in the range 3.5 GPa - 8.5 GPa, with an average of  $5.6 \pm 1.1$  GPa. These values correlated negatively with porosity (Fig. 14), i.e. low porosity samples respond in a stiffer manner. Temperature, pore fluid or sample size do not affect the observed trend. Average Poisson's ratios are  $0.06 \pm 0.04$ , and thus very low compared to typical range for sandstones of 0.25-0.35. Overall, compression of the samples during Segments A-B is likely resulting in closure of (micro)-cracks. Hence, Bulk Moduli (Segment A) and Poisson's Ratios (Segment B) are very low. No correlation was found with porosity, and high porosity samples display a relatively large spread in Poisson's ratios.

Note, that a number of UPPD studies reported in the past were executed with the first loading step included in the total UPPD loading cycle, instead of applying depletion from in-situ conditions. Those studies report relatively high values for uniaxial compressibility  $C_m$  (see Fig. 1, results for Ameland, Blija-Ferweradeel), as the strains measured also include first-loading crack closure.

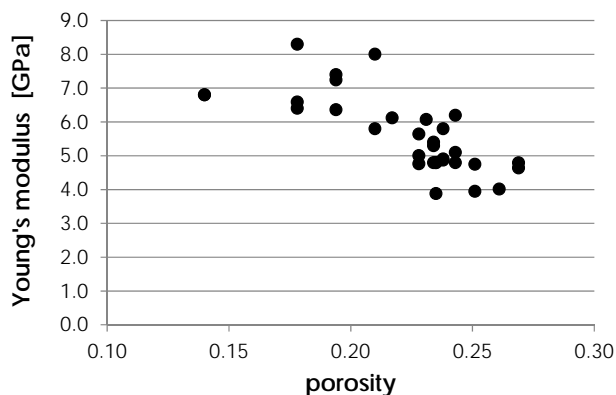


Fig. 14. Pre in-situ stress Young's modulus of MGT-3 samples as a function of the porosity.

From Constant Net Stress loading to in-situ stress (Segment C - Fig. 7), the solid phase or grain modulus  $K_s$  was calculated using the change in volumetric strain as a function of change in pore pressure. The average value for  $K_s$  found in this segment amounts to  $35.1 \pm 8.1$  GPa. This value approaches the static value for pure quartz (in the range 32 - 36 GPa), and gives confidence that pre-loading has indeed re-consolidated the sample to its previous in-situ state. For rocks with porosity, the Biot-Willis coefficient  $\alpha$  can be determined using the bulk modulus and grain modulus following the expression  $1 - K_b/K_s$ . Using the  $K_b$  and  $K_s$  values determined in segments A and C, an average value for Biot-Willis coefficient  $\alpha$  of  $0.97 \pm 0.01$  was found. Although this suggests that the effective stress ( $\sigma_e = \sigma_a - \alpha P_f$ ) can here be approximated by the Terzhagi effective stress, i.e.  $\sigma_e = \sigma_a - P_f$ , care must be taken as the true Bulk Moduli might be factors higher, and hence  $\alpha$  is expected to be lower. However, the choice for  $\alpha$  equal to unity does not affect the applicability of the experimental results to the field case. The applied axial stress employed in our tests is namely chosen on the basis of the magnitude of the overburden load, and hence independent of pore pressure. Furthermore, the analyses of the results obtained for the reference and special protocols (refer to Sections 3.3.3-3.3.5) are solely dependent on our choice of  $\alpha$ , and not on the other poroelastic constants reported in the present section.

#### 4.1.2. Axial strain and radial stress response to PPD

All samples were equilibrated to the newly restored stress conditions for 48 hours, after reaching the original in-situ stress state. Indeed, the axial strain attained after subjecting the sample to in-situ stress conditions is limited and stable before depletion commences (Fig. 13). The depletion stage, that then follows, results in axial strain that follows closely the pore pressure and radial stress changes. Note, that under the uniaxial boundary conditions chosen, the axial strain equals the bulk volumetric strain.

The pore pressure depletion stage resulted in axial strain that closely follows the pore pressure and radial stress changes. There is a positive trend with respect to porosity. Higher porosity samples resulted in more axial strain during the depletion stage. In Fig. 15, the axial strain obtained during pore pressure depletion versus porosity is shown. Note, the axial strain is taken over the whole depletion range so included the unload/reload cycles and creep accumulated over the depletion time period. Taking the secant of the axial stress-axial strain relationship of a particular depletion step yields the uniaxial compressibility  $C_m$  in  $\text{Pa}^{-1}$ , as introduced in Section 2. We can compute  $C_m$  for the full depletion stage, or per individual depletion step. In Fig. 17, we plot  $C_m$  versus each specific pore pressure depletion step, and, in Fig. 18,  $C_m$  for the first and the last depletion step for all samples, versus porosity. Two observations can be made. First, compressibility values roughly increase with increasing porosity for the final depletion step. Second, the compressibility decreases slightly as depletion progresses, as demonstrated by the slightly lower average values for the last depletion steps. The difference in  $C_m$  obtained for the first and last depletion step is shown in Fig. 17 where  $C_m$  is plotted versus porosity for all samples. Further, Fig. 18 shows that the average  $C_m$  in the first depletion step amounts to  $9.9 \cdot 10^{-5} \pm 1.3 \cdot 10^{-5} \text{ MPa}^{-1}$  while the average  $C_m$  of all samples in the last step is  $7.6 \cdot 10^{-5} \pm 2.3 \cdot 10^{-5} \text{ MPa}^{-1}$ . The decrease in compressibility indicates stiffening of the sample in progress of depletion. This stiffening is consistent with the trend in Young's modulus presented in Fig. 19, where the average Young's modulus of all samples in the first depletion step amounts to  $10.0 \pm 1.1 \text{ GPa}$  while the average Young's modulus of all samples in the last step is  $12.8 \pm 4.0 \text{ GPa}$ . Note that, in two cases, we have observed a sudden, slight in trend ("kink") in the stress-strain curve obtained for depletion. This kink is occurred at pore pressure of roughly 37 MPa, or slightly higher, with more compliant behavior in the high pore pressure range, and stiffer behavior at lower pressures. This could be an effect related to the virgin versus in-situ pore pressure during coring (refer to Table 1). Comparing now, the Young's Moduli obtained from first loading data (Fig. 14), with the data reported here in Fig. 19, demonstrates that the sample behaves in a stiffer manner during depletion, which again highlights the importance of reconsolidation during the first loading cycle to in-situ conditions of stress and pore pressure (refer to Section 4.1.1).

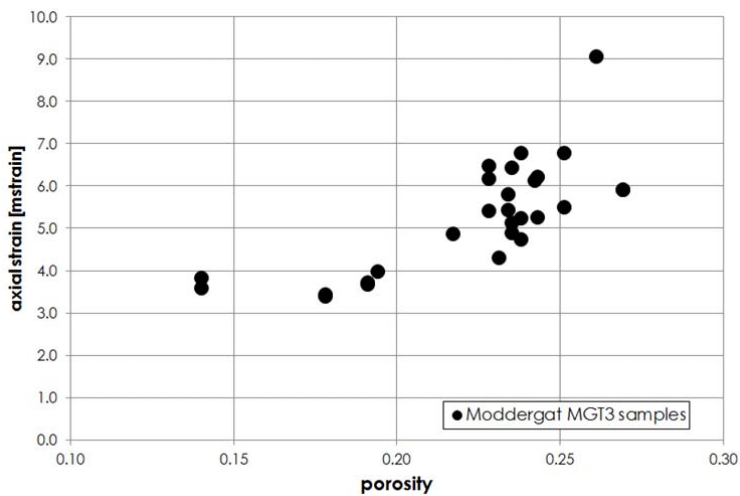


Fig. 15. Axial strain measured during depletion for all samples, and plotted versus porosity.

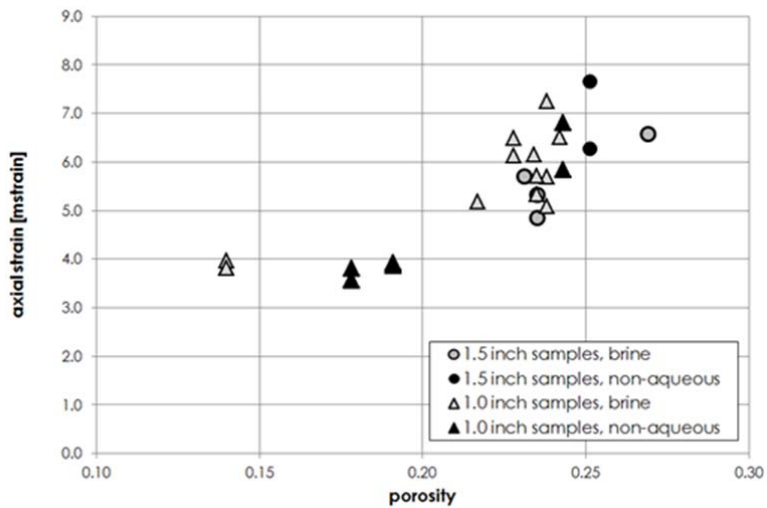


Fig. 16. Axial strain attained during depletion versus porosity, presented for 1.0" vs 1.5" diameter samples, and aqueous versus non-aqueous pore fluid.

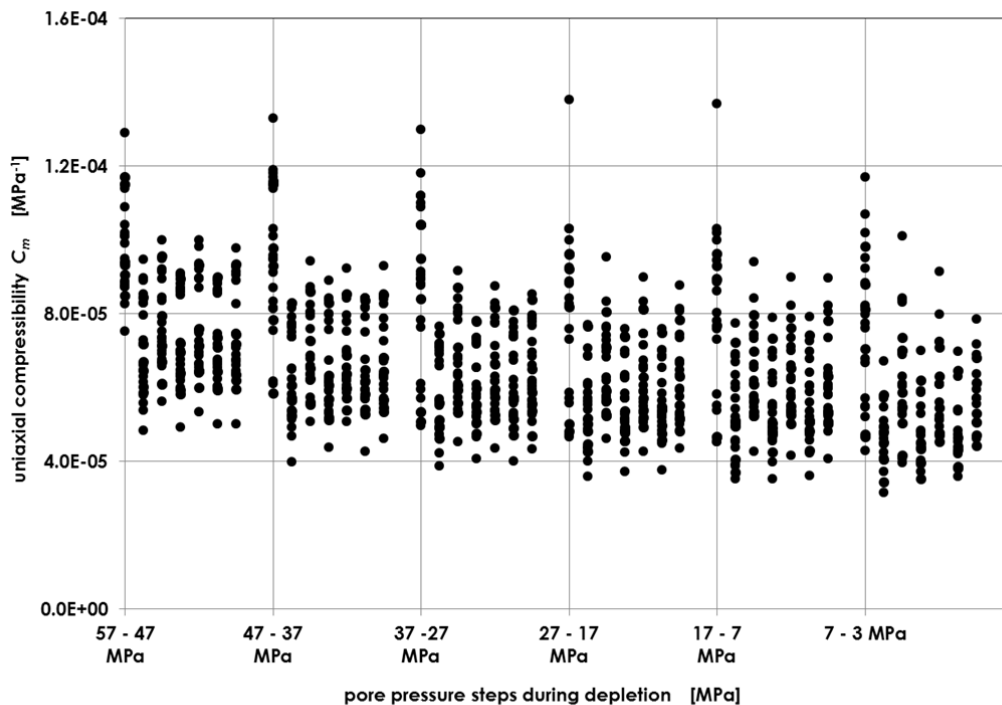


Fig. 17. Uniaxial compressibility  $C_m$  parameterized on the basis of the change in axial strain and pore pressure measured during all individual steps for all Moddergat-3 samples.

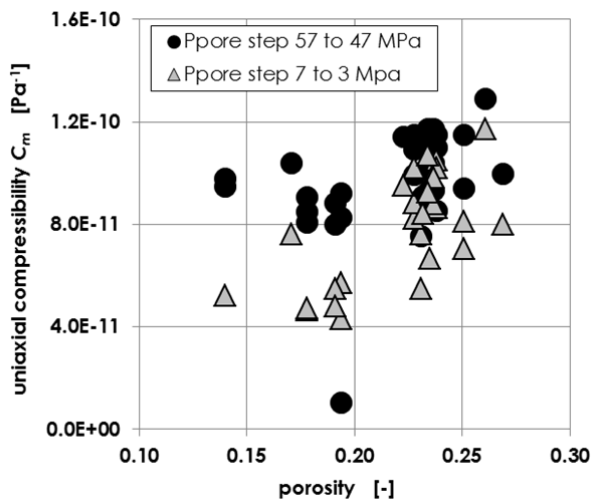
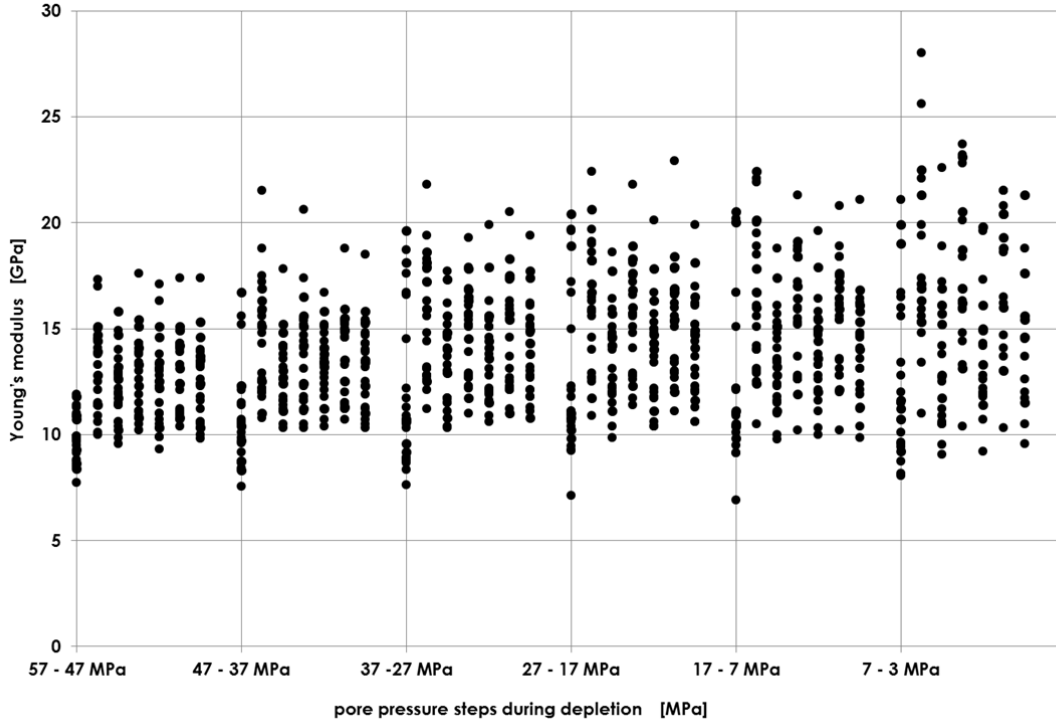


Fig. 18. Uniaxial compressibility  $C_m$  parameterized on the basis of the change in axial strain and pore pressure measured during depletion for all samples, and plotted versus porosity.



**Fig. 19.** Young's modulus measured during all individual pore pressure steps for Moddergat-3 samples, parameterized on the basis of measured 3D stress-strain data, and assuming linear poroelasticity.

In all experiments, the radial stress change during depletion varied between 20 and 27.5 MPa after reaching a maximum depletion pressure of 3 MPa (Fig. 20). The radial stress response shows no dependence on porosity. Using the change in radial stress response to the pore pressure change, we can compute the uniaxial (horizontal) depletion path constant  $\gamma_b$  following the general expression,

$$\gamma_h = \frac{\Delta S_{rad}}{\Delta P_p} \quad (1)$$

where  $\Delta S_{rad}$  is the change in radial stress over the depletion in MPa, in response to the change in pore pressure  $\Delta P_p$  in MPa. Taking  $\Delta S_{rad}$  and  $\Delta P_p$  during the first and the last depletion step, the depletion path constant was calculated and plotted as a function of porosity in Fig. 21. Clearly,  $\gamma_b$  decreases as depletion continues, i.e. progressively smaller radial stress changes were observed in these samples during depletion. In contrast to the uniaxial compressibility  $C_m$ , the depletion constant  $\gamma_b$  shows no noticeable dependence on porosity.

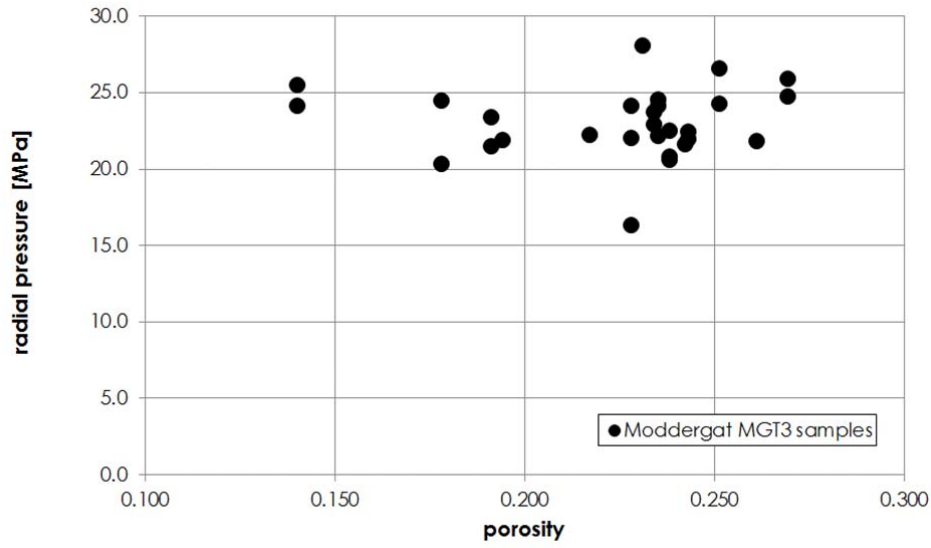


Fig. 20. Change in radial stress over the full depletion cycle for all samples, plotted versus porosity.

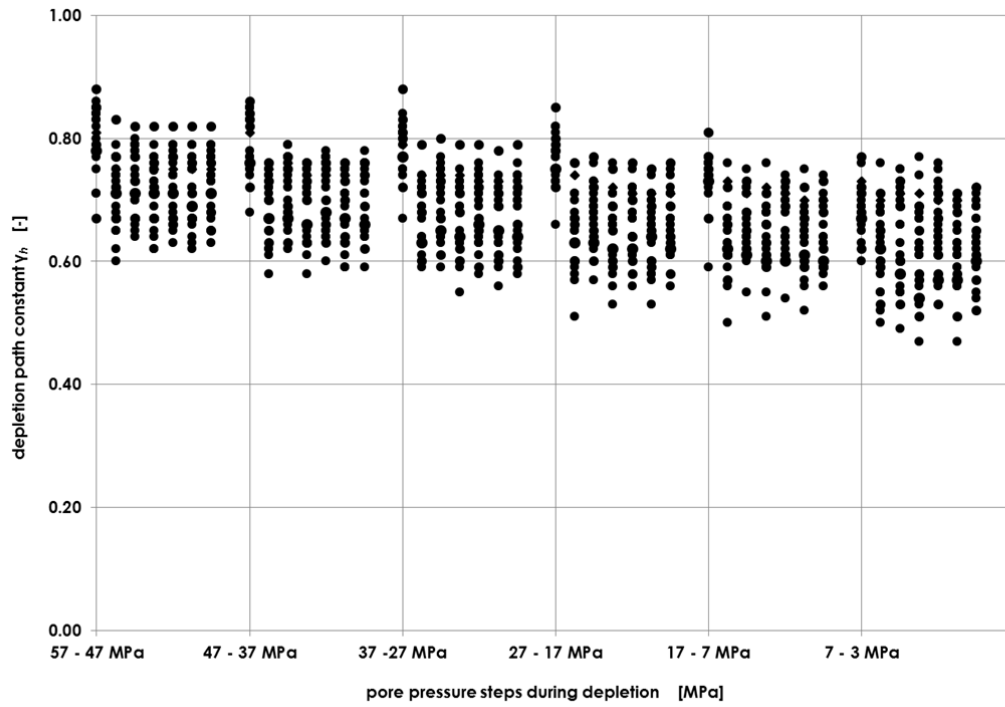


Fig. 21. Depletion path constant  $\gamma_h$  parameterized on the basis of the change in radial stress and pore pressure measured during all individual steps for all Moddergat-3 samples.

#### 4.1.3. *Axial stress hold – Uniaxial creep strain*

The pore pressure depletion stage was followed by a hold period of at least 300 hours. The hold period was performed under uniaxial strain boundary conditions. The hold period under uniaxial strain conditions was followed by a 72 hours period under triaxial stress conditions. Three tests (MGT3-30E, MGT3-34A and MGT3-34B) were performed with a hold period of at least 1500 hours. Creep data are presented in Fig. 22, where the axial strain is plotted as a function of time for the hold period for all samples. All samples showed a monotonic axial strain increase over time, similar to the response seen in Fig. 13 for sample MGT-22A. Additional strains of  $5 \cdot 10^{-4}$ - $15 \cdot 10^{-4}$  were attained at 300 hours. Strain rates continuously decreased over time.

Time-dependent compaction shows a positive correlation with porosity; higher porosity resulted in more compaction of the sample during the hold period. The reason why the axial strain acquired with sample MGT3-34C is much higher compared to the other samples is not known. In Fig. 23, the axial strain obtained during the hold period under uniaxial strain boundary conditions is plotted as a function of porosity. The fractions presented in Fig. 27 hence represent the contribution of time-dependent strain to the total strain, at the time scale of the experiment. These data show that the (rapid) pressure-depletion employed in our tests results in at least 80% of the total strain response being close to instantaneous, and less than 20% time-dependent. Time-dependent behavior is more persistent in samples with a high porosity.

Besides the range of sample porosities, changes in experimental conditions were applied with respect to temperature, pore fluid, stress path. The relationship between the attained axial strain and changes in experimental conditions are weaker than obtained with porosity. The following trends were found:

- Pore fluid: Samples with non-aqueous pore fluids show slightly more compaction. During the creep stage compared to samples with brine as pore fluid (Fig. 24).
- Temperature: There is no clear relationship between compaction and temperature (Fig. 25). In some experiments, the amount of axial strain attained increased with increasing temperature while in another experiments an opposite effect is seen.

In total, five long-duration experiments with a hold period under uniaxial strain boundary conditions of at least 1500 hours have been performed. The axial strain attained during the hold period as a function of time is presented in Fig. 26. In the experiment with sample MGT3-34B, malfunctioning of the radial displacement transducer forced us to stop the test after 1800 hours. All samples showed an axial strain increase over time with decreasing strain rate. For sample 30E, the axial strain rate was decrease to zero after 2500 hours and maintaining stable conditions for 1000 hours. For sample MGT3-34A, the strain rate at 2500 hours and beyond was  $10^{-11} \text{ s}^{-1}$  or slower. It is well-accepted that strain rates beyond  $10^{-11} \text{ s}^{-1}$  are difficult to measure as control systems are less reliable.

Finally, we observe from the data presented in Fig. 13 that there is close to zero radial stress change required to maintain uniaxial strain boundary conditions during the final hold period. Changes in radial stress are solely significant during the pore pressure depletion stage.

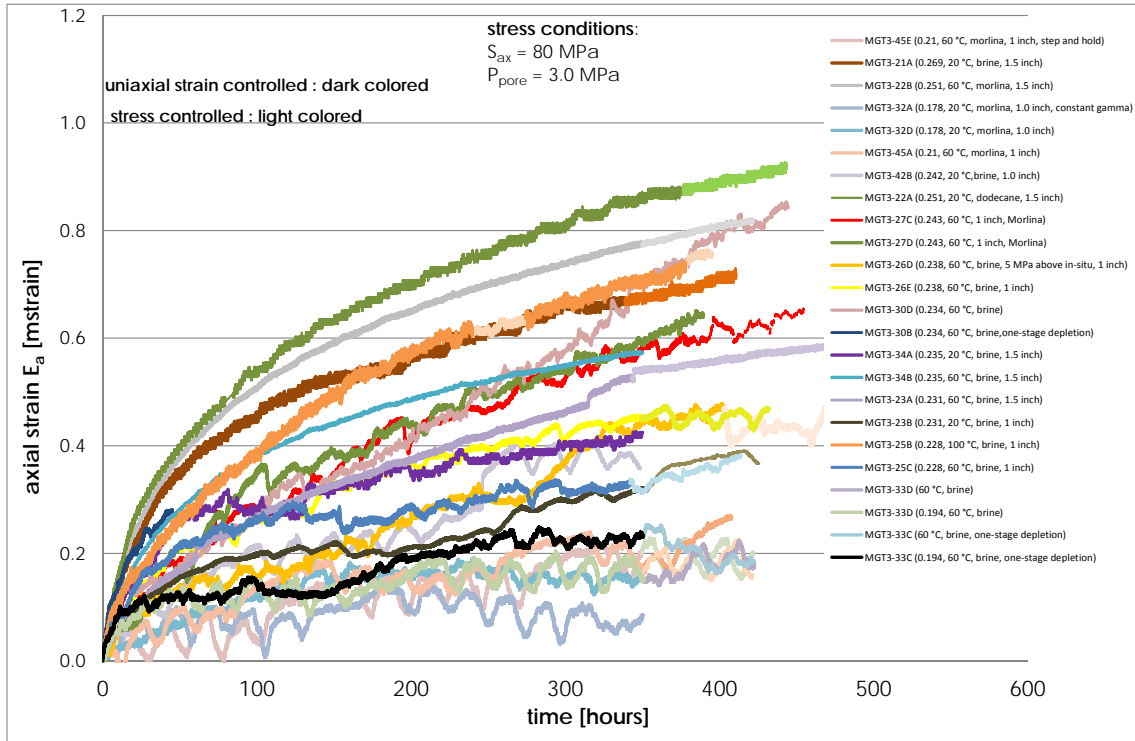


Fig. 22. Axial strain acquired during hold period at maximum depletion conditions for all Moddergat MGT3 samples. Note that the fluctuations were caused by variations in laboratory temperature.

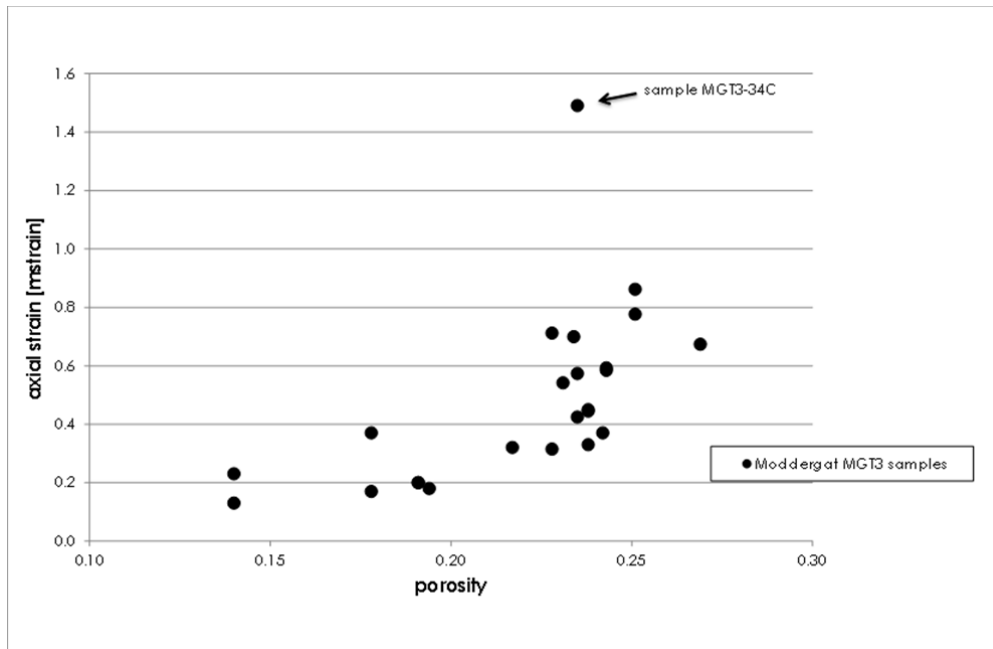


Fig. 23. Axial strain attained during the 350 hrs hold period under uniaxial strain conditions versus porosity.

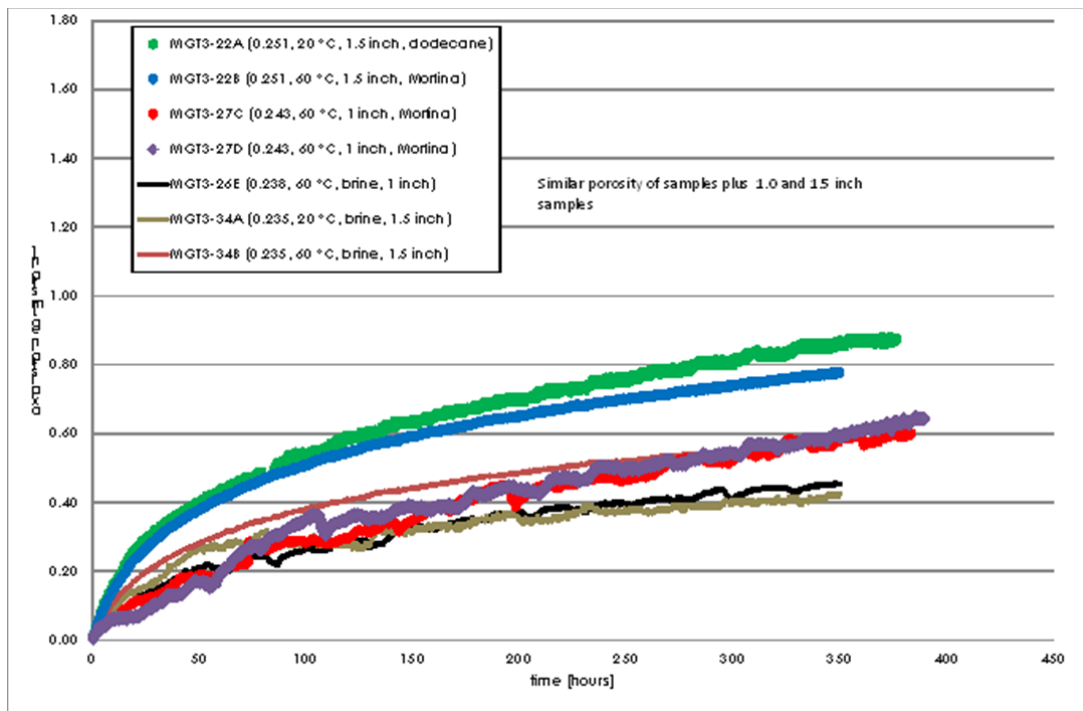


Fig. 24. Axial strain attained during the 300 hrs hold period under uniaxial strain conditions as a function of time for samples with aqueous and non-aqueous pore fluid.

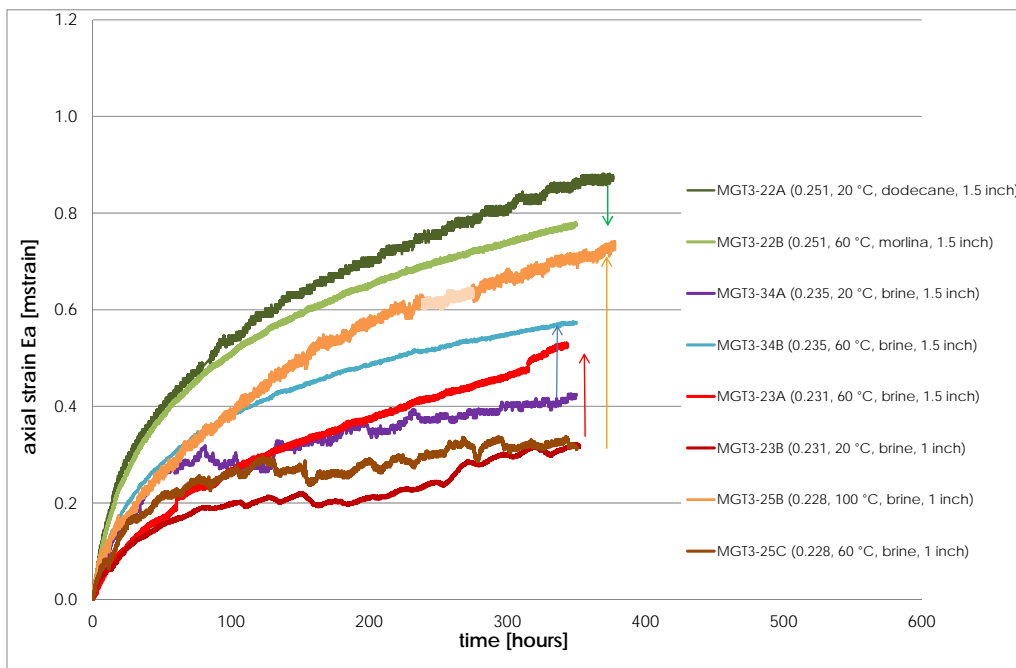


Fig. 25. Axial strain attained during the 300 hrs hold period under uniaxial strain conditions as a function of time for samples subjected to pore pressure depletion followed by a hold period at different temperatures.

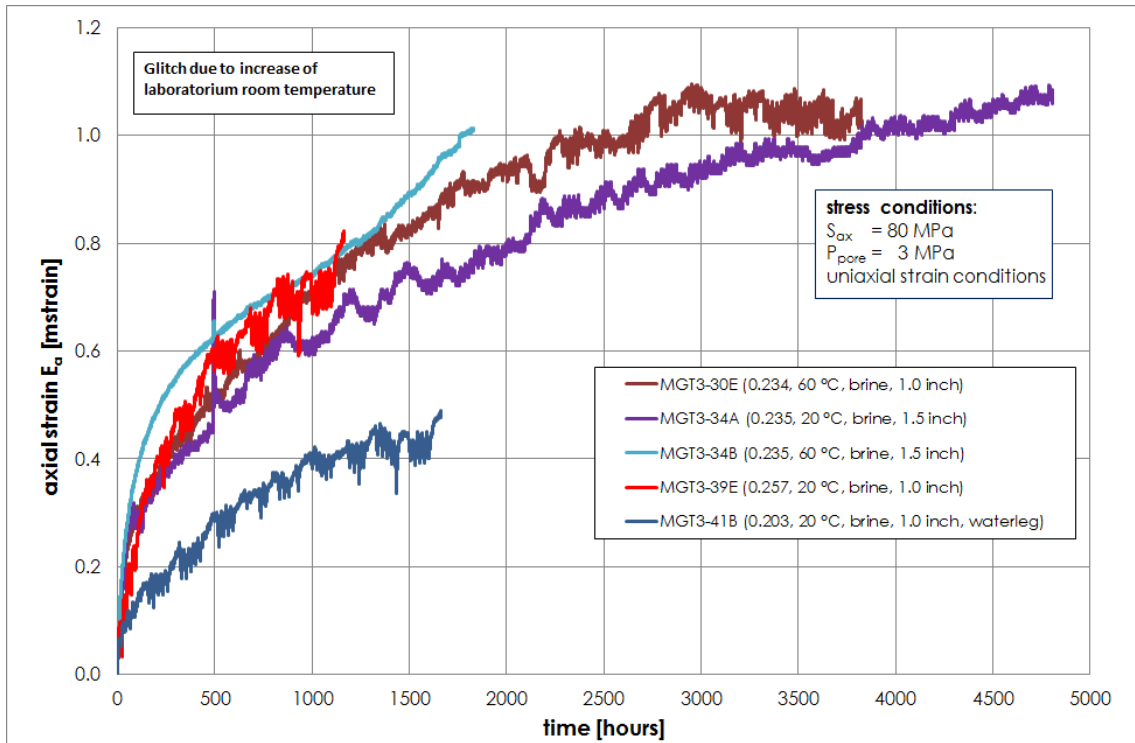


Fig. 26. Axial strain attained during the long-duration hold period under uniaxial strain conditions as a function of time for samples MGT-34A, MGT-34B, and MGT-30E.

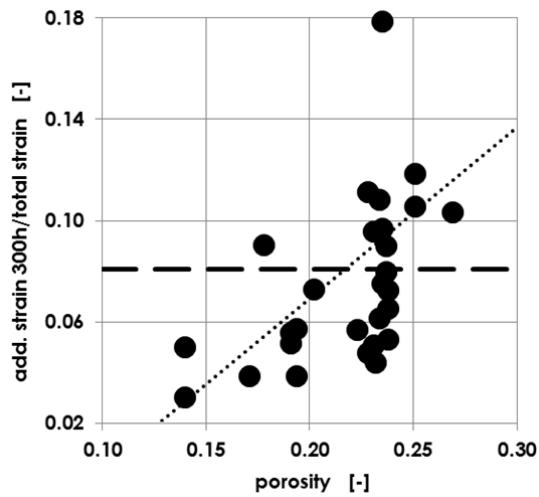
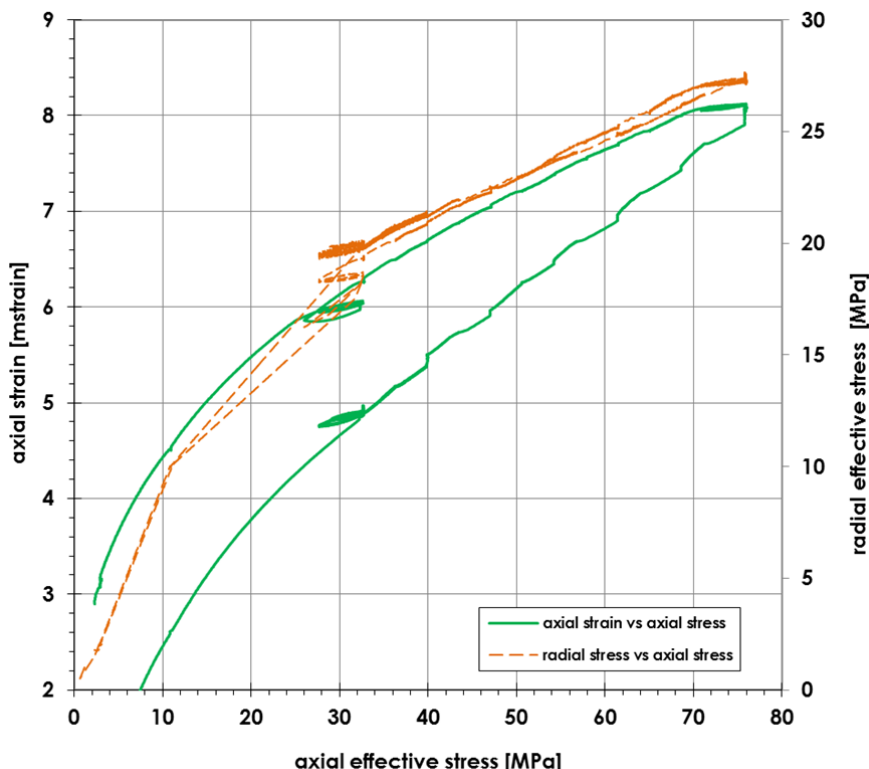


Fig. 27. Fraction of time-dependent strain in 300 hours after depletion to total strain versus porosity for all samples.

#### 4.1.4. Special protocols: Rate-type behavior and Stress-free strain conditions

The oedometric loading protocol described in Section 3.3.4, performed on two samples MGT3-35D and MGT3-35E, resulted in strain response plotted in Fig. 28. The response to axial loading under drained, zero pore pressure conditions and a temperature of 60 °C, resulted in roughly  $4 \cdot 10^{-3}$  axial strain, which was recoverable for roughly  $\frac{2}{3}$ . By contrast, the radial stress response required to maintain zero-lateral strain conditions, was fully recoverable. The varying loading rates of  $0.3 \text{ MPa}\cdot\text{hr}^{-1} \rightarrow 3 \text{ MPa}\cdot\text{hr}^{-1} \rightarrow 0.3 \text{ MPa}\cdot\text{hr}^{-1} \rightarrow 30 \text{ MPa}\cdot\text{hr}^{-1} \rightarrow 0.3 \text{ MPa}\cdot\text{hr}^{-1} \rightarrow \text{etc.}$  resulted in a strain response directly following the stress change in the case of slow loading of  $0.3 \text{ MPa}\cdot\text{hr}^{-1}$ , and a smaller immediate response plus a creep component in the case of fast loading of  $30 \text{ MPa}\cdot\text{hr}^{-1}$ . However, note that this contrasting behavior is seen only in the case of loading, and barely during unloading. Hence, the loading-rate dependent strain response must be related to the inelastic strain attained.



**Fig. 28.** Axial strain versus stress data for special protocol to investigate rate-type behavior. Experiment using sample MGT-35D with a porosity of 0.182. Note, that this interval was also tested from compressive strength, which will be reported in Section 4.2.

Two experiments (using samples MGT-36B and MGT-39B) were performed where the material was depleted under so-called ‘stress-free strain’ boundary conditions, i.e. where the externally applied stress remains unperturbed while the sample is subjected to pore pressure decrease and undergoes its intrinsic volume strain, with the aim to establish deviations from isotropic, linear-elastic behavior. Following the equilibration period for 48 hours, the axial and radial stresses were kept constant at in-situ stresses (80 MPa and 67 MPa respectively) while the pore pressure was decreased in a stepwise manner.

The depletion stage, results in axial and radial strain that follows closely the pore pressure changes. During the depletion stage, for both stress-free strain experiments, the amount of radial strain of  $7 \cdot 10^{-3}$  is roughly double the axial strain of  $3 \cdot 10^{-3}$ . A reference experiment was carried out performing a standard UPPD stress path with sample MGT3-39E. During the uniaxial pore pressure depletion, an axial strain (=volumetric strain) of  $5.7 \cdot 10^{-3}$  was attained, which is  $\frac{1}{3}$  of the volumetric strain attained in the stress-free strain experiment.

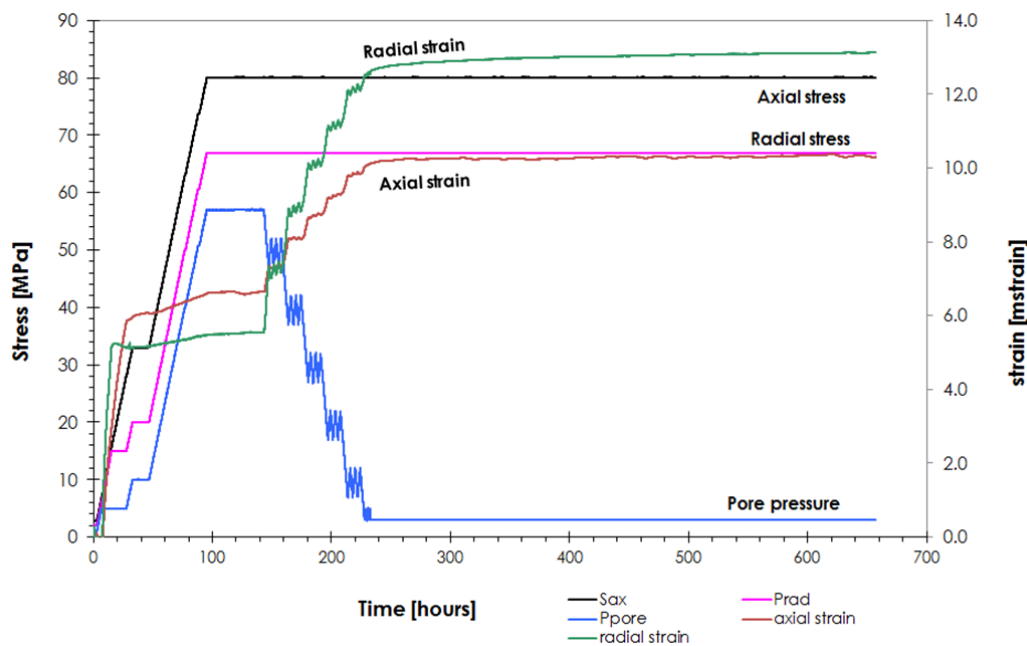


**Fig. 29. Stress-free strain stress path, in this case sample MGT-39B. The sample is brought to virgin in-situ stress, and subjected to a decrease in pore pressure while maintaining constant axial and radial stress. Measured responses are the axial and radial strain.**

The bulk modulus  $K_b$  per individual depletion step was determined by using the mean stress and volumetric strain data. In Fig. 30, we plot  $K_b$  versus each specific pore pressure depletion step. Two observations can be made. First, the bulk modulus increases as depletion progresses. The increase in bulk modulus indicates stiffening of the sample in progress of depletion. This stiffening is consistent with the trend in Young's modulus found in the UPPD experiments (described in Section 4.1.2). Second, the bulk modulus determined in the unload cycles is larger than the load cycles. This represents the contribution of inelastic strain. This finding is in line with the trend found in the UPPD experiments.

By applying linear elastic theory, the bulk modulus can be derived from the depletion steps in reference experiment MGT-39E by using Young's modulus and Poisson's ratio to derive  $K_b$  with formula:  $K_b = E/(3(1-2\nu))$ . The calculated  $K_b$  values are shown in Fig. 30. The calculated values come more in line with the experimentally derived  $K_b$  in progress of depletion.

After the depletion stage, the stress conditions were maintained for at least 350 hours. In this stress hold period, the amount of radial strain was  $\sim 3$  times the amount of axial strain (Fig. 31). When sample MGT3-39B is compared to Moddergat sample MGT3-39E, the amount of volumetric strain acquired during the hold period under triaxial stress conditions is twice the axial (= volumetric) strain during the hold period under uniaxial strain conditions.

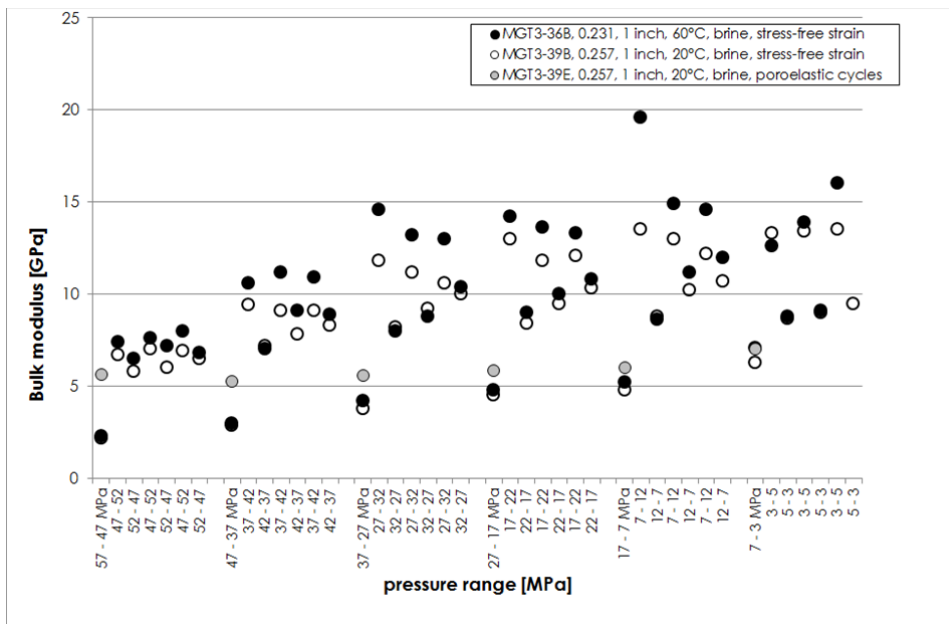


Fig. 30. Bulk modulus  $K_b$  parameterized on the basis of the change in mean stress and volumetric strain measured during all individual steps in stress-free strain experiment and reference UPPD experiment MGT3-39E.

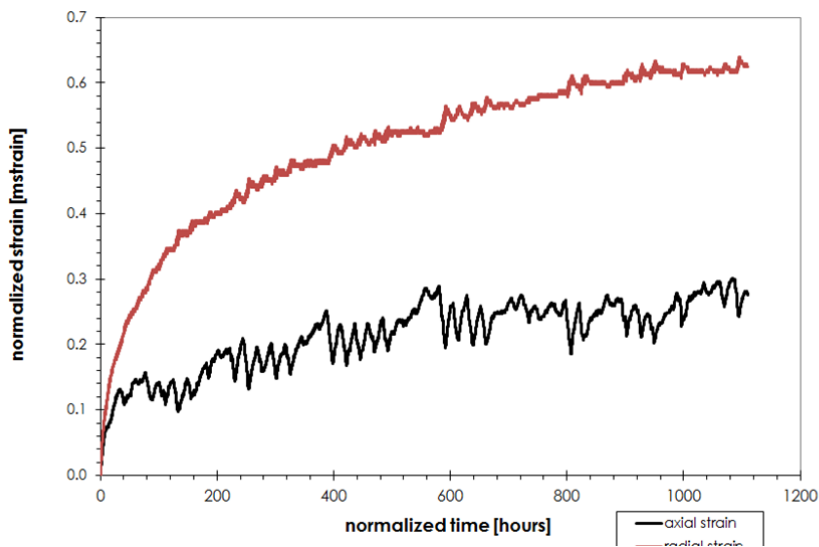


Fig. 31. Axial and radial strain acquired during hold period at maximum depletion conditions for sample MGT3-39B. Note that the fluctuations were caused by variations in laboratory temperature.

## 4.2. Triaxial compressive strength data

The peak failure point is taken as the maximum deviator stress the sample can handle before failure. From this point, the mean effective stress  $p'$  and deviator stress  $q$  are calculated using the expressions  $p' = [\text{axial effective stress} + \text{radial effective stress}]/2$ , and  $q = [\text{axial effective stress} - \text{radial effective stress}]/2$ , and listed in Table 3, as well as presented graphically in Fig. 32 for the two series of triaxial tests. Also are indicated the two tested samples that were saturated with a non-aqueous fluid (Samples MGT-24D and MGT-31).

The sample set with the lowest porosity of 0.14, shows the highest strength, with a friction angle of  $42.1^\circ \pm 3.1^\circ$  and cohesion of  $8.2 \pm 2.1$  MPa (see also Table 4). By contrast, the sample set having a high porosity of 0.27 displays a lower friction angle of  $33.7^\circ \pm 5.0^\circ$ , but a similar cohesion of  $7.8 \pm 3.5$  MPa. The friction angles obtained compare very well with those reported in the literature by *e.g.* Chang et al. [4] as a function of porosity. For the two sets, the Unconfined Compressive Strength (UCS) was calculated using the obtained friction angles and cohesion, and results in 29.3 MPa for set MGT-24 and 36.9 MPa for set MGT-29 (see Table 4).

Ultrasonic velocity measurements show a transition from a gradual decrease in travel times during the first  $\frac{2}{3}$  of the loading path to an increase in travel times, marking the transition from compressional to dilatant behavior at the onset of failure. This effect was observed for all samples tested, and is marked in Fig. 32 using open circles. Prior the pre-failure loading the bulk modulus was determined by a 4 MPa unloading and loading cycle (Table 5). In addition to the peak failure data, the stress-strain data between  $\frac{1}{3}$  and  $\frac{2}{3}$  of the total curve to shear failure were also taken to assess the Young's modulus (Table 5). Lateral strains, and hence Poisson's ratio, measured by means of the two-pin strain sensor, could not be determined reliably as dilation and failure are also directionally dependent.

**Table 3: Summary of triaxial compressive strength data for the MGT-3 samples**

sample	depth [m]	porosity [%]	S <sub>ax</sub> [Mpa]	S <sub>rad</sub> [Mpa]	P <sub>pore</sub> [Mpa]	from stresses		from velocities		test conditions	pore fluid
						p' [Mpa]	q [Mpa]	p' [Mpa]	q [Mpa]		
24A	3827.37	27	53.4	7.1	5.0	30.3	23.2	25.7	18.6	0.5 VMES	brine
24B	3827.37	27	81.4	14.3	5.0	47.8	33.5	38.3	24.0	1 VMES	brine
24E	3827.37	27	89.9	17.8	5.0	53.9	36.0	42.6	24.8	1.25 VMES	brine
24D	3827.37	27	89.7	14.3	5.0	52.0	37.7			1 VMES	dodecane
29A	3840.09	14	75.1	7.1	5.0	41.1	34.0	31.5	24.4	0.5 VMES	brine
29B	3840.09	14	108.2	14.3	5.0	61.2	46.9	44.0	29.8	1 VMES	brine
29E	3840.09	14	53.3	3.5	5.0	28.4	24.9	24.6	21.1	0.25 VMES	brine
31C	3822.33	22	42.1	3.6	5.0	22.8	19.3	19.1	15.5	0.25 VMES	Blandol oil
35A start	3819.84	18	80.0	27.3	3.0	50.7	26.4			at max. depletion	brine
35A	3819.84	18	80.0	11.0	3.0	42.5	24.9			ramp S <sub>rad</sub> -2.5MPa/h	brine
35B start	3819.84	18	80.0	23.9	3.0	49.0	28.1			at max. depletion	brine
35B	3819.84	18	80.0	12.5	3.0	43.3	33.8			tertiary creep	brine

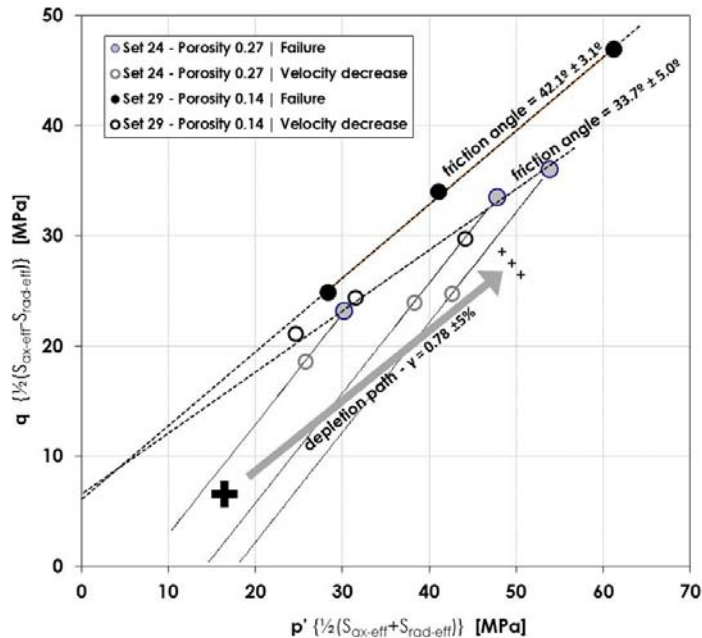


Fig. 32. P-q plot presenting triaxial strength data for two sample sets with the end-member porosities of 0.14 and 0.27. Note, the lower friction angle for the samples with a porosity of 0.27, and the expected worst-case depletion stress trajectory on the basis of  $\gamma_h=0.78$ .

Table 4. Friction angle and apparent cohesion for the MGT-3 samples

sample series	depth [m]	porosity [%]	friction angle [deg]	+/- [deg]	cohesion [Mpa]	+/- [Mpa]
24	3827.37	27	33.7	5.0	7.8	3.5
29	3840.09	14	42.1	3.1	8.2	2.1

Table 5. Bulk and Young's moduli of the MGT-3 samples

sample	depth [m]	porosity [%]	Kb [Mpa]						E [GPa]
			cycle 1		cycle 2		cycle 3		
			unload	load	unload	load	unload	load	
24A	3827.37	27	1.9	2.2					5.0
24B	3827.37	27	1.6	1.9	4.1	3.8			7.9
24E	3827.37	27	1.9	1.9	4.6	4.2	5.9	5.5	8.3
24D	3827.37	27							8.0
29A	3840.09	14	2.9	2.9					11.8
29B	3840.09	14	2.4	2.3	7.2	6.2			14.1
29E	3840.09	14	0.9	0.7					8.6
31C	3822.33	22							5.4

## 5. Discussion

The relatively high porosity and permeability of the samples tested (Fig. 2) explains why Permian reservoirs in North Netherlands region are major producers. Because of this high permeability, we are confident that pore pressure equilibration can be achieved rapidly, and hence the pore pressure decrease employed in the present experiments can be relatively fast. In this section, we will address the mechanical response of the Permian sandstone to depletion under uniaxial strain boundary conditions, by focusing first on the axial strain, and then on the radial stress response. Because the changes in strains measured were less sensitive to temperature and pore fluid composition than the applied stress and porosity, we will focus primarily on the role of porosity and particle size distribution in the constitutive response to depletion.

### 5.1. Total compaction and elastic-inelastic strain partitioning

The trend seen in the elastic properties parameterized on the basis of our mechanical data, namely that stiffening occurs during depletion, clearly suggest that a densification mechanism operates, and hence that a portion of the strain measured is inelastic. The term “compressibility”, used in the Geertsma model introduced in Section 2, and more widely applied in the industry, is merely taken as a parameterization of stress-strain data obtained, and bears no *a priori* relation to the recoverability of the response [as described in detail in the monographs 5, 6]. However, for understanding the origin of subsidence from a rock constitutive standpoint, there is a clear need to focus on strain partitioning during depletion, and in particular the temporal and spatial nature of this.

To assess the various strain contributions, we took the mechanical data of five representative tests performed on samples with porosities ranging from 0.14 to 0.27, and separated the total strain measured during the loading-unloading cycles of each depletion step (refer to Section 4.1.2) into elastic and inelastic strain. Note, that the differences in strain response observed between the reference stress path (protocol in Section 3.3.2) and the one-step depletion stress path (protocol in Section 3.3.3) are within the variability of the data set, which demonstrates that stress cycling has no observable impact on the nature of the deformation. The elastic strain attained during the three inflation cycles of 5 MPa visible in each depletion step, were averaged and extrapolation to the full step of 10 MPa (*i.e.* the elastic strains were averaged and multiplied by a factor two). We now plot in Fig. 33 for the representative, high-porosity sample MGT-22A, the total, elastic and inelastic strain components as a function of the mean pore pressure during each depletion step. As pore pressures reduce during depletion, the trends should be read right-to-left. We then plot in Fig. 34, the relative contribution of inelastic strain to the total depletion strain, versus porosity for all five samples considered. Note, that the analysis excludes the strains developed during the final hold period. Fig. 33 shows that the contribution of inelastic strain in sample MGT-22A is monotonically increasing during depletion and amounting to  $\sim 5.5 \cdot 10^{-3}$ . Indeed, Fig. 34 shows that samples with a high porosity exhibit up to  $\frac{3}{4}$  inelastic strain (*i.e.*  $\frac{3}{4}$  permanent strain, assuming no viscoelastic response), and low porosity samples show an opposite elastic-inelastic balance. The data suggest that for a porosity of 0.2, representative for the Permian sandstone reservoir considered here, the total strain response is roughly  $\frac{1}{2}$  elastic and  $\frac{1}{2}$  inelastic. Taking a closer look at the absolute magnitudes (not plotted), reveals that the elastic response is fairly porosity-independent in comparison with the inelastic response that strongly increases with porosity.

Projecting now forward the contribution of inelastic strain to approach a value of 1.0 (Fig. 34), which would represent the point where the sample is expected to deform solely inelastically, a porosity range of 0.3-0.4 is reached. Although the elastic strains in the samples could also increase with porosity as predicted on the basis of Hertzian contact mechanics, the trend

presented here for a material having a fairly similar grain size distribution throughout the sample set, is consistent with idea that packing differences lead to the intensification of the external axial stress at local grain contacts in high-porosity samples. Assuming that strength at the grain contacts is a material property, and hence local strength is independent of porosity, stress intensification will promote local failure in high-porosity samples. The “maximum” porosity reached of 0.3-0.4 would indeed be consistent with the idea that the microstructural texture is, in fact, a close-packing structure where the porosities are dependent on the packing type, as well as particle size distribution, and that these properties govern deformation.

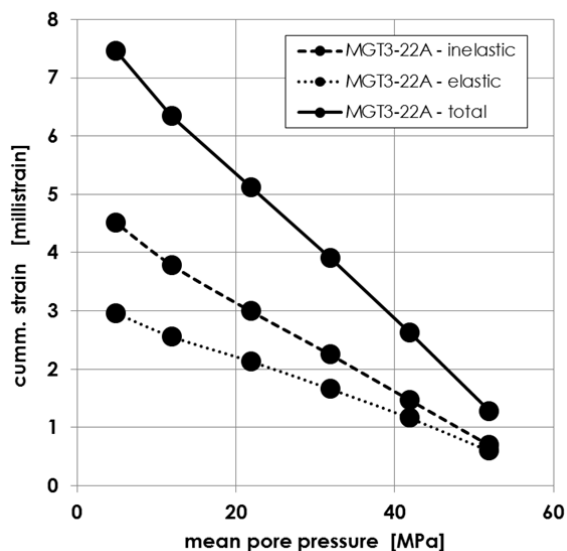


Fig. 33. Elastic-inelastic strain partitioning versus mean pore pressure for Sample MGT-22A with a porosity of 0.25.

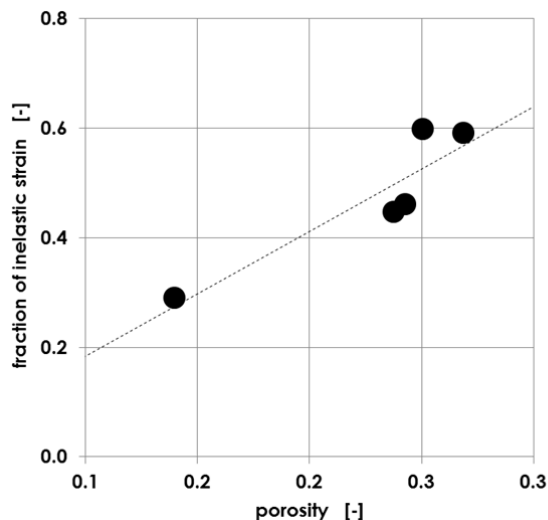


Fig. 34. Contribution (fraction) of inelastic strain to total strain after full depletion for five representative samples versus their respective porosity. Note, that the trend projects to a fully inelastic strain (*i.e.* 1.0 on the y-axis) at values of porosity between 0.3 and 0.4, which would be in agreement with maximum porosities for close-packing structures.

Turning now to the effect of strain partitioning on the radial stress response, we recall that the depletion path constant  $\gamma_b$ , which assumes a linear elastic response of a rock to pore pressure changes (*e.g.* [5]), is classically expressed as,

$$\gamma_h = \frac{\Delta S_h}{\Delta P_p} = \alpha \frac{(1-2\nu)}{(1-\nu)} \quad (2)$$

Taking now the most ideal values for such systems of  $\alpha=1$ , and  $\nu=0.25$ , Eq. 2 predicts a  $\gamma_b$  of  $\sim 0.66$ , which agrees reasonably with the depletion path constants found in our tests ( $\gamma_b=0.6-0.75$ ) on the basis of the change in radial stress and pore pressure during the last depletion stage. Although the first-order model, field-derived values for  $\gamma_b$ , and the laboratory-derived  $\gamma_b$ -values for the 7-3 MPa depletion step show reasonable agreement, the 57-47 MPa step yields values for  $\gamma_b$  in the range 0.7-0.9. These numbers are too high for the ideal linear elastic case considered above, suggesting a gradual decrease in magnitude of the radial stress change over the course of depletion. In addition to the evolution of  $\gamma_b$  from high to low values, the radial stress changes closely follow the imposed pore pressure change during depletion, whereas the time-dependent axial strain response seen in the hypoplastic cycles during depletion, as well as the final, long hold period, do not seem to correlate with that radial stress response (Fig. 13). From this, we infer that the first-order elastic behavior is solely captured in the data as an instantaneous response, and hence the depletion path constant  $\gamma_b$  appears rather insensitive to porosity. Inter-granular movement in the material, which results in the porosity-dependent inelastic strain, is more persistent in the first steps of the depletion, and results in an apparent higher depletion path constant. Progressive compaction consolidates and stiffens the material, hence decreasing  $\gamma_b$  to more realistic “linear elastic” values of 0.6-0.75.

## 5.2. Deformation mechanisms responsible for inelastic strain

The densification of sedimentary rock during progressive burial in the upper crust is generally caused by (a combination of) mechanical compaction (cracking, sliding) [*e.g.* 7], and chemical lithification (pressure solution, cementation) [*e.g.* 8], and results in a decrease in porosity. Both classes of mechanisms result in inelastic strain, either instantaneous or time-dependent.

The limited sensitivity of the mechanical data to temperature and pore fluid chemistry rules out a strong contribution of (chemical) dissolution-precipitation mechanisms. By contrast, the strong role grain packing plays in the deformation of our samples (Fig. 34), and the fact that the uniaxial deformation clearly decelerates during the final hold period (Fig. 13, Fig. 22-Fig. 26), suggests that grain failure/re-arrangement is the most likely mechanism responsible for the inelastic deformation observed, which would confirm the observations made recently by Post et al. [9] for Rotliegendes sandstone from the Groningen Field, and by Schutjens [10] who reported compaction of quartz sand below  $\sim 300^\circ\text{C}$  to occur primarily by granular cracking, and dissolution-precipitation mechanisms at higher temperatures.

To microstructurally identify the operative deformation mechanism, we have performed SEM analysis using untested samples (taken from the core material, between the plugs), and compared the images with those of plug material post-testing (refer to Section 3.3.8). Fig. 35 displays a representative SEM image of undeformed material within interval MGT-26. Visible grains size between  $\sim 20\ \mu\text{m}$  and  $\sim 300\ \mu\text{m}$  in 2D cross-sectional view, which is consistent with the particle size distributions obtained (Fig. 3). A fraction  $\sim 0.9$  of the grains is composed of quartz, and  $\sim 0.1$  of K-feldspar and plagioclase. Lower porosity samples contain uncracked anhydrite as a pore filling phase (refer to Appendix A6.5). Focusing now on images in Fig. 36 and Fig. 38 of the plug samples after mechanical testing, shows no evidence for local catastrophic collapse or abundant grain indentation. This gives confidence that pore collapse and pressure solution creep can be

ruled out as dominating mechanisms, and explains the lack of sensitivity of the strain response to depletion on temperature and pore fluid chemistry. Table 6 lists the number of cracked grains in the microstructures presented in Fig. 36 (post-testing) versus Fig. 35 (pre-testing), and similarly compared microstructures for other samples, and shows that the samples in the post-testing state contain up to a total fraction 0.22 more cracked grains. We then plot in Fig. 37, the increase in cracked grain fraction as a function of porosity. A possible increase in cracked grain fraction with porosity can be observed. The detailed microstructure presented in Fig. 38 of sample MGT-26E (post-testing) highlights that a) most cracks initiate at grain contacts, b) the cracks run parallel to the applied stress during mechanical testing, and c) frequently have an en-echelon nature locally. From these observations, we infer that active cracking has occurred during mechanical testing, and is likely responsible for the strain measured. The limited translation and rotation of the cracked grains is consistent with the small strains observed during the tests. A simple calculation of the number of grains per average sample (using: porosity=0.2, total volume of 1" sample= $2.5 \cdot 10^{-5} \text{ m}^3$ , mean grain size=220  $\mu\text{m}$ , mean grain volume= $5.6 \cdot 10^{-12} \text{ m}^3$ ) yields  $\sim 9 \cdot 10^5$  grains per sample. If an average fraction of 0.1 of the grains is being cracked during the test, then a typical total volumetric strain during depletion of  $1 \cdot 10^{-5}$ , and hence an axial displacement of 50  $\mu\text{m}$ , results in a shortening of  $(50 / (0.1 \cdot 9 \cdot 10^5)) = 5.6 \cdot 10^{-4} \mu\text{m}$  per cracked grain. The contribution of these individual small strains to bulk deformation cannot be measured and upscaled with the analytical techniques that are available to date.

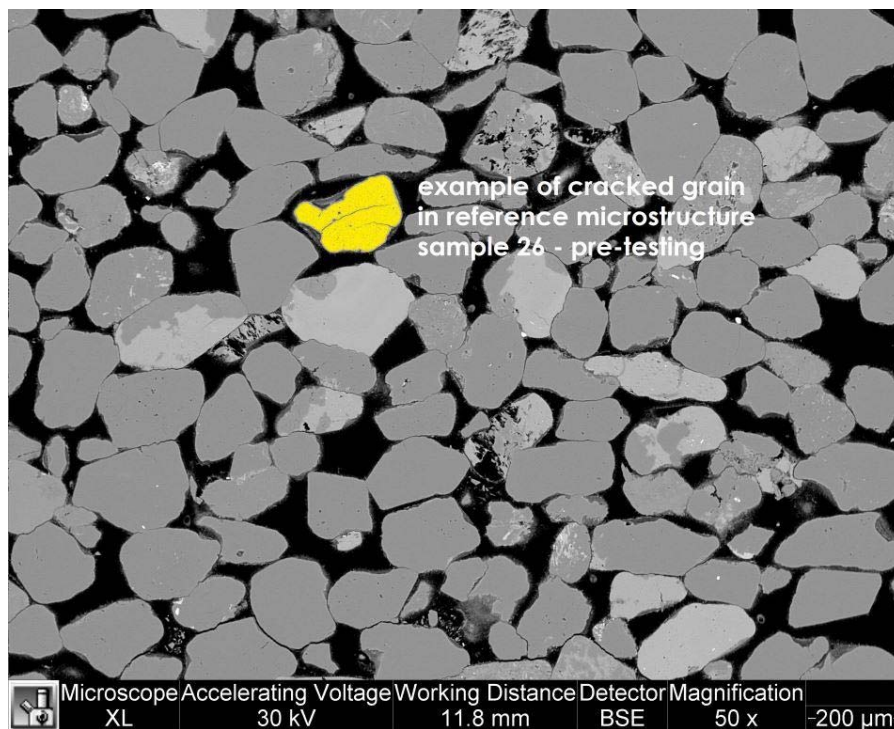


**Fig. 35.** SEM image of undeformed material within interval MGT-26, taken directly from the core, between the plug locations. The section is oriented with the normal of the plane in the strike direction of the layering, with top-bottom vertically. Note, that the undeformed material contains a number of cracked grains.

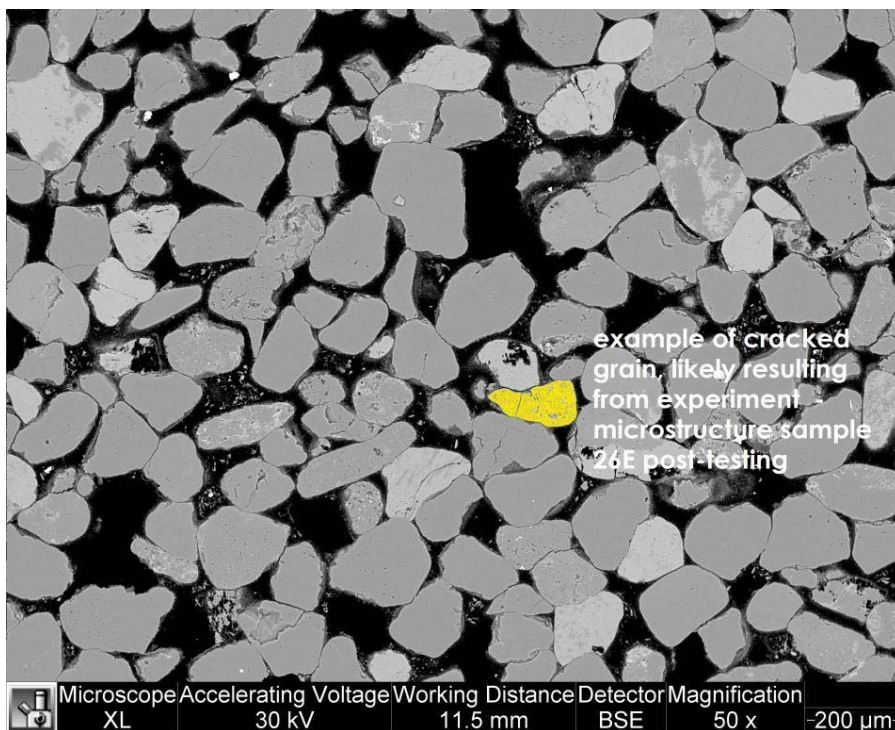


Fig. 36. SEM image of sample MGT-26E in the deformed state.

SAMPLE	POR	QTZ		KFS+PLAG				
		TOTAL	CRACKED	FRACTION	TOTAL	CRACKED	FRACTION	TOTAL FRACTION
PRE								
27	0.243	214	11	0.05	13	1	0.08	0.05
21	0.269	130	2	0.02	25	2	0.08	0.03
22	0.251	114	20	0.18	15	4	0.27	0.19
26	0.238	121	12	0.10	15	4	0.27	0.12
29	0.140	196	24	0.12	18	7	0.39	0.14
POST								
27D	0.243	135	14	0.10	27	7	0.26	0.13
21A	0.269	128	10	0.08	23	5	0.22	0.10
22A	0.251	ND	ND		ND	ND		
26E	0.238	127	40	0.31	20	10	0.50	0.34
29D	0.140	195	31	0.16	21	7	0.33	0.18
DIFFERENCE								
27D-27	0.243			0.05			0.18	0.08
21A-21	0.269			0.06			0.14	0.07
22A-22	0.251							
26E-26	0.238			0.22			0.23	0.22
29D-29	0.140			0.04			-0.06	0.03

Table 6. Result of counting number of cracked grains in microstructures of samples MGT-26 and MGT-26E presented in Fig. 36 (post-testing) versus Fig. 35 (pre-testing), and various other samples.

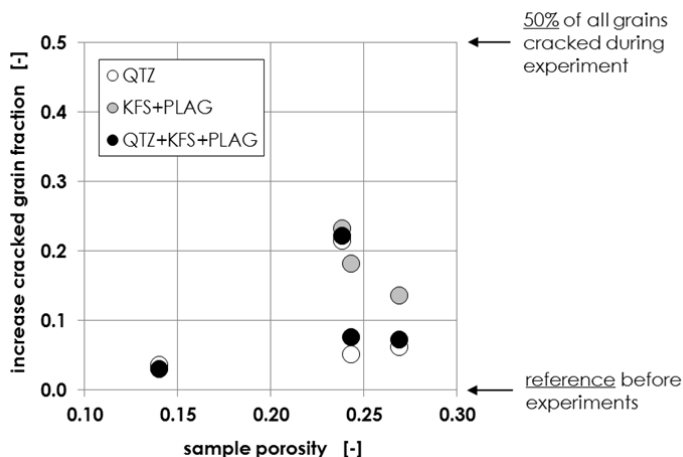


Fig. 37. Fraction of cracked grains in SEM images of samples post- versus pre-testing.

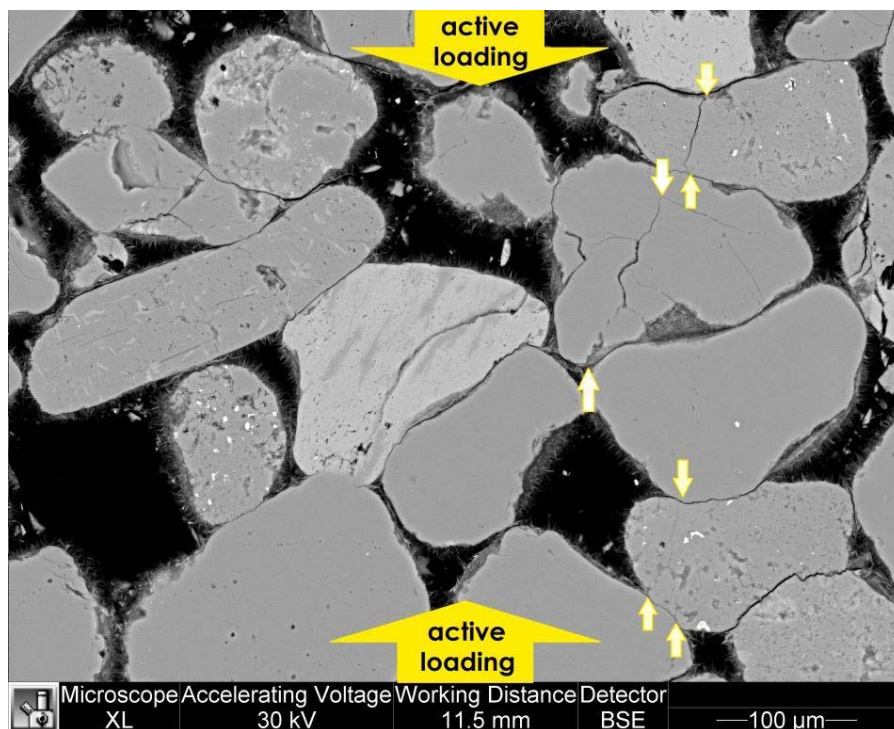
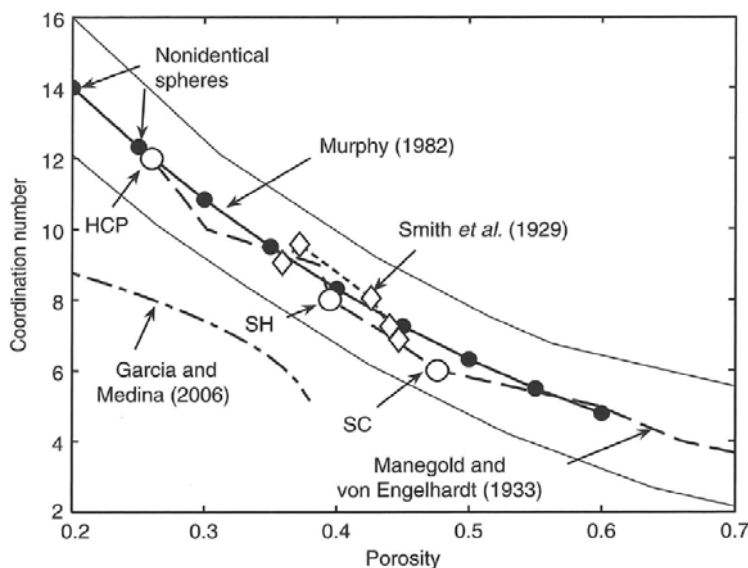


Fig. 38. SEM image of sample MGT-26E in the deformed state, as in Fig. 36, now at higher magnification.

Focusing on the contributions of (elastic) compression and time-independent and time-dependent (inelastic) grain cracking, studies by e.g. Brzesowsky et al. [11], Wong and Baud [12], Heap et al. [13, 14] and Brantut et al. [15, 16] report experimental and modeling results that support our findings for the conditions chosen here. Brzesowsky et al. [11] developed an analytical model for single particle size grain packs, which predicts the contributions of time-independent, elastic and inelastic strain by considering the inter-particle force distributions in the pack, and their elastic response, assuming specific elastic properties for the contacts, or local strength in the case of inelastic strains. Although the natural sandstones used in this study are

very well sorted, and generally exhibit clean, single-mode particle size distributions (Fig. 3 and Fig. 4), the distribution itself, as well as internal heterogeneity (banding) may prove application of the above model problematic. Nonetheless, we will below qualitatively consider the role of packing during deformation. Since deformation of the granular aggregates is determined by local stress on the grain contacts, and hence the number of contact points (expressed as the “coordination number”, c.n.), and their area, the packing differences can lead to a competition between two mechanical effects, namely a) the absolute size of the particles that determine the number of contact per unit cross-sectional area, and b) the width of the distribution promoting densification and hence the number of contact points per unit cell.



**Fig. 39. Coordination number versus porosity for various packing arrangements (SC=simple cubic, SH=simple hexagonal, HCP=hexagonal close packing). Note that the HCP structure is densest packing possible. Source: Mavko et al. (2009).**

Mavko et al. [17] present a plot showing the relationship between coordination number and porosity for various spherical particle packing geometries (Fig. 39). For a single-mode grain packing, the hexagonal close packing structure represents the densest possible arrangement, and has a porosity of  $\sim 0.26$ . Lower porosity arrangements can be achieved only by means of mixing grains of different size into the pack. This naturally results in an increase of the coordination number. For the porosity range of the Permian sandstones samples used here of 0.14-0.27, packing of single-sized grains is not possible, as confirmed by the distributions presented in Fig. 3. Rough extrapolation of the trend in Fig. 39 predicts, for the porosity range of our samples, coordination numbers ranging from 11.7 for a porosity of 0.26, to 15.8 for a porosity of 0.14. The general trend in grain size distribution of the samples (refer to Section 3.2 and Fig. 4) indeed confirms this prediction, as higher porosity samples tend to have a smaller mean grain size, and a narrower log-normal distribution.

Based on the packing trend considered here, we expect that for a given, fixed change in external applied stress during depletion, the contact forces in the sandstone are greatest in samples with a low coordination number, i.e. within the samples with a narrow grain size peak and a high porosity. Returning now to the model by Brzesowsky et al. [11], and examining in their paper the effect of packing arrangement (SC versus SH) on the contribution of inelastic to the total strain, we see that a greater contribution of inelastic strain in the case of a simple cubic packing (fraction 0.820, c.n. = 6) compared to simple hexagonal packing (fraction 0.776, c.n. = 8) for the applied external stress of 22 MPa. In Fig. 40, we compare the modeled contributions with the strains

presented in Fig. 34 for our samples, and plot these against porosity, as well as indicate on a secondary axis the corresponding coordination numbers. From the trend, we observe a close to linear dependence of inelastic and coordination number on porosity, and from that we infer the available theory related to packing, and the available models for grain cracking can adequately describe inelastic strain as observed in our samples. As grain cracking is fundamentally caused by exceeding a critical stress level required to fail an individual grain, the largest inelastic strains at a given applied effective stress can be observed in grain packs with a low coordination number, i.e. in samples with a narrow grain size distribution.

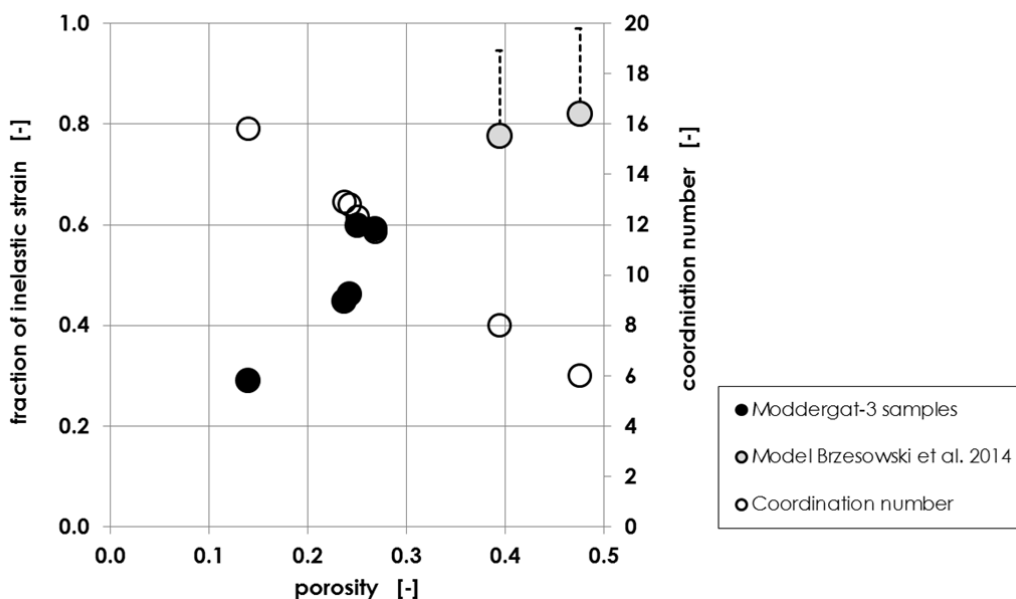


**Fig. 40.** Fraction of inelastic strain for Moddergat samples compared with analytical model by Brzesowsky et al. 2014. The magnitude of error bars in the Brzesowsky is purely suggestive, and accounts for the difference in effective external loading (77 MPa for the present study, versus 22 MPa for Brzesowsky et al.). Secondary axis refers to corresponding coordination number c.n. (number of contacts per spherical particle). The c.n. for Moddergat samples has been extrapolated from the trend reported by Mavko for single grain packs and mixtures, as presented in Fig. 39, and represents the mean for the distribution. The plot clearly suggests that the measured inelastic strain is strongly related to packing.

It not entirely clear from the present data if the cracking of grains observed is related to the time-independent strains only, or also to the time-dependent strains. Notably, the studies by Heap et al. [13, 14] and Brantut et al. [15, 16] have shown that brittle creep can occur in (consolidated) sandstone as a result of stress corrosion cracking [cf. 18]. These authors show that the strain response to differential loading related to the operation of the latter mechanism is dependent on pore fluid chemistry, as well as temperature. The first, because it is physically interacting with the solid at pre-existing, stressed crack tip surfaces, and the latter, because it controls the chemical activity of the fluid. In our experiments, a dependence on fluid chemistry or temperature is not clearly observed. Although this topic clearly requires further investigation, we note that there are several differences between the experiments reported here, versus those by Heap et al. [13, 14] and Brantut et al. [15, 16]. First, the pore fluids used in our experiments are expected to be less chemically active in quartz, as they are oils, or saturated brine solutions. Second, our experiments were performed under conditions of zero or positive strain (uniaxial strain boundary conditions), where the authors mentioned employ 3D stress that can result in a dilatant state.

### 5.3. Role of lateral boundary conditions – strain versus stress control

An ultimate consequence of the microscale failure mechanisms considered in the previous section, and an inaccurate understanding of the lateral boundary conditions, could be that the progression of local damage promotes catastrophic failure of the samples.

To highlight this problem, we first qualitatively compare in Fig. 32 the rock strength determined via triaxial compression, with the expected stress trajectory from the virgin in-situ effective stress in the reservoir to the final stress state in depleted conditions, using a worst-case experimentally obtained value for  $\gamma_b$  of  $0.78 \pm 0.05$ , the rock strength determined, as well as the onset of microscale failure affecting the ultrasonic wave propagation, are clearly separated from the inferred stress path by several MPa. In a well-understood case, it is therefore unlikely that grain failure and re-arrangement during pore pressure depletion under uniaxial-strain boundary conditions results in shear failure, and hence that depletion under uniaxial strain conditions can be achieved within the mechanically stable regime. However, uncertainty in the applicability of the lateral constraint as a boundary condition to the relatively small fields present in the Wadden Area, re-raises potential concerns with regards to stability, and urges for execution of tests dedicated to the role of lateral boundary condition. The abovementioned studies by Brzesowsky et al. [11], Heap et al. [13, 14], and Brantut et al. [15, 16] are all conducted on either unconsolidated sand in an oedometer, or using sandstone under triaxial stress conditions. To the knowledge of the authors, no data exist that actively vary boundary conditions from uniaxial strain to triaxial stress control at maximum depletion, and hence two additional experiments were carried out on sandstone samples MGT-35A and MGT35B from the sample interval with a porosity of 0.18 to assess the sensitivity of sample failure to changes in lateral boundary conditions after depletion. These tests follow initial stress path stages identical to those reported in Sections 3.3.2 for most other samples (*i.e.* the stages: triaxial loading to in-situ stress, and depletion under uniaxial strain conditions), but in this case the axial stress hold stage that follows was not performed under uniaxial strain boundary condition, but instead by decreasing the radial stress at a fixed rate of 2.5 MPa/hr, either in one step (Sample MGT-35A), or in several small steps of  $\Delta\sigma_{rad} = -0.5$  MPa or  $-1.0$  MPa (Sample MGT-35B). In doing this, the deviatoric stress increased stepwise until close to failure, and then followed by holding the stress constant provoking tertiary creep until failure occurred. These tests were performed at 60°C constant. The tests both result in failure (condition listed in Table 3) slightly below the trend found for sample set MGT-29 (Fig. 41). If we recall that the porosity of set MGT-29 is around 0.14, then the obtained data for the present experiments on set MGT-35 with a porosity of 0.18 is fully consistent. Focusing now on the development of strain rate close to the point at which shear failure occurs, we note from Fig. 42 for Sample MGT-35B that strains clearly accelerate towards failure. However, the absolute stress difference between this point and the projected compressive strength on the basis of the data presented in Fig. 32 is less than a couple of MPa, *i.e.* at absolute stresses above the onset of microscale damage inferred from the ultrasonic measurements. In order words, the changes in ultrasonic properties of the samples (indicated with open circles in Fig. 32) are indeed bounding the conditions where microscale damage occurs, but this damage does not readily lead to catastrophic failure.

The above considerations suggest that even though the samples have gone through a full depletion cycle, and microscale grain cracking may have taken place, the inherent compressive strength appears relatively unaffected.

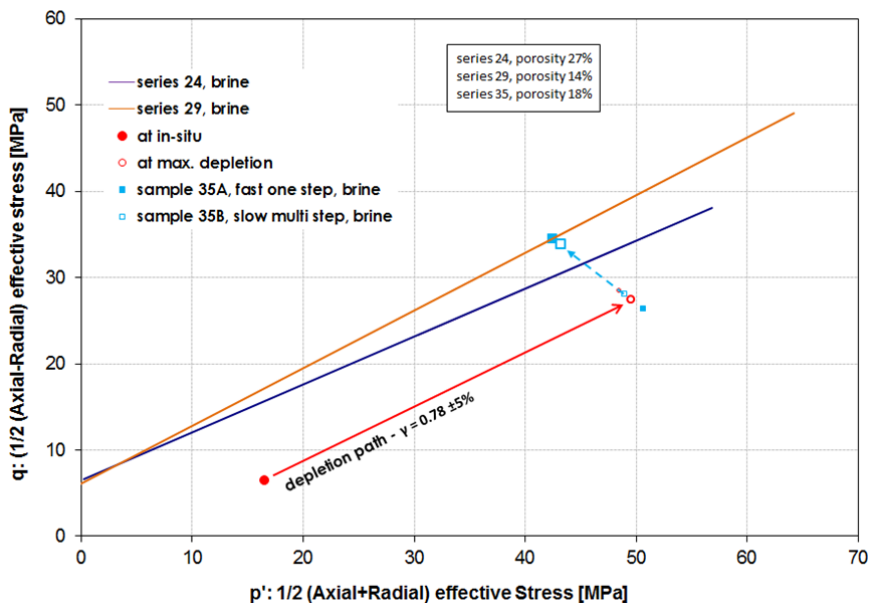


Fig. 41. Compressive strength test of sample 35A and 35B at the end of the depletion

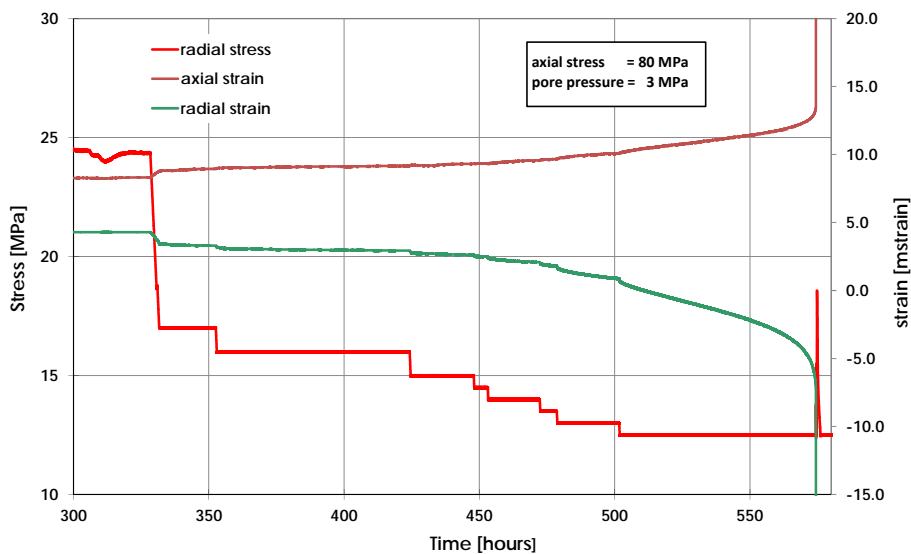


Fig. 42. Axial strain and radial strain in time for Sample MGT-35B, in response to the stepwise decrease of radial stress (constant:  $S_{ax} = 80$  and  $P_p = 3$  MPa). Note the acceleration of axial and radial strain, i.e. an increase in strain rate as radial unloading progresses.

#### 5.4. Upscaling of laboratory tests

The most simple manner in which upscaling of our findings to the field scale can be achieved, is to take a column of rock with a representative reservoir thickness of 50 m, and applying the obtained total average strains to compute the total shortening of the column via the expression  $\Delta L = \epsilon_{tot} \cdot L_0$ . This oversimplified approach yields a total 20-60 cm of shortening in the reservoir, which is closely consistent with the magnitude of surface subsidence measured using levelling techniques that locally amount to 0-40 cm to date. Considering that 30-70% of the deformation in our samples is inelastic, the Geertsma(-derived) models can potentially be used only to geometrically upscale compaction to subsidence.

While our data show that more than 80% of the deformation is closely following pressure decline, field data suggest a time lag of several years. The existence of such a time lag is not unique to the Wadden Sea area [19], but the underlying mechanisms are poorly understood to date. Such mechanisms could relate to salt plasticity or water-leg compaction, and are under scope within the current Wadden Sea research program.

Various (semi-)analytical models have been proposed in the literature, and have been used actively by NAM and others, to history-match and/or forward-predict subsidence on the basis of laboratory rock compaction, or levelling data. For example, a recent review of such models [20] treats the soft soil isotach model, the stress-linearized isotach model, the standard Linear Solid (SLS) model, its special version, the time-decay model, and finally, the Rate Type Compaction Model. Without going into the mathematical details of the models, comparing the data presented in this report to the predictions made by the models is challenging for various reasons which we will qualitatively consider. First, the models are one-dimensional, and as such no 3D constitutive equations, whereas the results presented in our study demonstrate an important role of lateral boundary conditions (zero lateral strain versus constant 3D applied stress during depletion). Second, the models are empirical, and are, as such no micromechanical constitutive equations. Consolidated, cemented sandstones are cohesive by nature and are hence capable of sustaining deviatoric stresses to some extent. This cohesion results in a resistance to stress, and hence dictates the magnitude and 3D nature of the stress-strain response. These sandstones cannot be compared with unconsolidated soils under axial loading for the sake of simplicity. Third, the models do not assume a priori knowledge on the elastic versus inelastic strain partitioning, as found in our experiments, and can hence be fit successfully to the experimentally determined stress-strain data only in one loading direction, unless mechanical properties are actively changed after loading. Considering the above arguments, we recommend (on the long term) developing 3D constitutive theory, that a) has a micromechanical, physical basis applicable to consolidated sandstones, and b) is capable of incorporating elastic and inelastic processes. For the purpose of hypothesis testing on the short term, linear extrapolation of the average, worst-case creep rate must be taken as bounding the present time-dependent reservoir response.

## 6. Conclusions

This study investigated the constitutive behavior of the Permian reservoir sandstones, and, in particular, the magnitude of the strain response to stress changes, as well as their temporal nature. We have carried out a large number of triaxial and UPPD tests. The outcome of our study can be summarized as follows:

- (i) Pore pressure depletion and associated densification in our samples is positively correlated with porosity, with total strain amounting to  $5 \cdot 10^{-3}$  -  $15 \cdot 10^{-3}$  after 5-12 weeks. Inelastic strain increases with porosity, and comprises  $\frac{1}{2}$  of the total strain response for a representative porosity of 0.2.
- (ii) 80% of the total strain response is close to instantaneous, and measured during depletion itself. Maximum 20% strain is time-dependent.
- (iii) Microscale contact mechanics, and associated elastic and inelastic behavior, is responsible for the compaction-compression response observed in our experiments.
- (iv) Volumetric compaction of the Permian sandstone reservoir could be responsible for the magnitude of the subsidence, but it cannot directly explain the observed temporal relationship between subsidence and reservoir pressure decline, or at least not without some rescaling factor. Instead, other mechanisms such as salt flow or water-leg compaction should also be considered.
- (v) We recommend (on the long term) developing 3D constitutive theory, that a) has a micromechanical, physical basis applicable to consolidated sandstones, and b) is capable of incorporating elastic and inelastic processes. For the purpose of hypothesis testing on the short term, extrapolation of the creep strain taking an average, worst-case strain rate must be taken as bounding the present time-dependent reservoir response.
- (vi) Additional experimental testing focusing more on the role of boundary conditions and strain rate could be beneficial for constraining applicable models and their parameters.

## References

1. Geertsma, J. 1973. Land subsidence above compacting oil and gas reservoirs. *Journal of Petroleum Technology*. 25: p. 734-744.
2. Geertsma, J. 1973. A basic theory of subsidence due to reservoir compaction: The homogeneous case. *Verhandelingen Koninklijk Nederlands Geologisch en Mijnbouwkundig Genootschap*. 28: p. 43-62.
3. Zoback, M.D., *Reservoir Geomechanics*. 2010, Cambridge: Cambridge University Press. 449.
4. Chang, C., M.D. Zoback, and A. Khaksar. 2006. Empirical relations between rock strength and physical properties in sedimentary rocks. *Journal of Petroleum Science and Engineering*. 51: p. 223-237.
5. Wang, H.F., *Theory of linear poroelasticity with applications to geomechanics and hydrogeology*. 2000, Princeton: Princeton University Press. 287.
6. Zimmerman, R.W., *Compressibility of Sandstones*. Developments in Petroleum Science. 1991: Elsevier. 173.
7. Zhang, J., T.-F. Wong, and D.M. Davis. 1990. Micromechanics of pressure-induced grain crushing in porous rocks. *Journal of Geophysical Research: Solid Earth*. 95: p. 341-352.
8. Rutter, E.H. 1983. Pressure solution in nature, theory and experiment. *Journal of the Geological Society*. 140: p. 725-740.
9. Post, A.D., et al., *Creep in Groningen Sandstone*. 2010, Shell International Exploration and Production B.V.: Rijswijk. p. 58.
10. Schutjens, P.M.T.M. 1991. Experimental compaction of quartz sand at low effective stress and temperature conditions. *Journal of the Geological Society*. 148: p. 527-539.
11. Brzesowsky, R.H., et al. 2014. Time-independent compaction behavior of quartz sands. *Journal of Geophysical Research: Solid Earth*. 119: p. 2013JB010444.
12. Wong, T.-f. and P. Baud. 2012. The brittle-ductile transition in porous rock: A review. *Journal of Structural Geology*. 44: p. 25-53.
13. Heap, M.J., P. Baud, and P.G. Meredith. 2009. Influence of temperature on brittle creep in sandstones. *Geophysical Research Letters*. 36: p. L19305.
14. Heap, M.J., et al. 2009. Time-dependent brittle creep in Darley Dale sandstone. *Journal of Geophysical Research: Solid Earth*. 114: p. B07203.
15. Brantut, N., et al. 2012. Micromechanics of brittle creep in rocks. *Journal of Geophysical Research: Solid Earth*. 117: p. B08412.
16. Brantut, N., et al. 2013. Time-dependent cracking and brittle creep in crustal rocks: A review. *Journal of Structural Geology*. 52: p. 17-43.
17. Mavko, G., T. Mukerji, and J. Dvorkin, *The Rock Physics Handbook - Tools for Seismic Analysis of Porous Media*. 2009, Cambridge: Cambridge University Press.
18. Atkinson, B.K. and P.G. Meredith, *The theory of subcritical crack growth with applications to minerals and rocks*, in *Fracture Mechanics of Rock*. 1987, Academic Press Inc.: London.
19. Hettema, M., E. Papamichos, and P. Schutjens. 2002. Subsidence Delay: Field Observations and Analysis. *Oil & Gas Science and Technology - Rev. IFP*. 57: p. 443-458.
20. Pruiksma, J.P., J.N. Breunese, and K. van Thienen-Visser, *A general framework for rate dependent compaction models for reservoir rock*. 2013, TNO: Utrecht. p. 49.